# Detailed simulation of dual-reflux pressure swing adsorption process

**Tushar S. Bhatt[a], Giuseppe Storti[b], Renato Rota[a,*]**

[a] *Politecnico di Milano, Chemistry, Materials and Chemical Engineering Department "Giulio Natta", Via Mancinelli 7, 20131 Milan, Italy*

[b] *ETH Zürich, Department of Chemistry and Applied Biosciences, Vladimir-Prelog-Weg 1-5/10, HCI F 125, 8093 Zürich, Switzerland*

## Highlights

- Aspen Adsim® model for simulating realistic DR-PSA process scenarios is presented.
- 19 experimental runs reported by McIntyre et al. (2010) are simulated.
- Model predictions are in good agreement with experimental results.
- Effect of feed position on process performance is assessed via simulations.

## Abstract

A model for the detailed simulation of dual-reflux pressure swing adsorption process developed in the frame of the commercial software Aspen Adsim® is presented. For validation purposes, simulations were performed and model predictions were compared with published experimental results. At cyclic steady-state, model predictions were found to be in good agreement with reported experimental results in terms of: (i) average ethane mole fraction in heavy product, (ii) average nitrogen mole fraction in light product, (iii) instantaneous heavy product composition profiles, and (iii) instantaneous column composition profiles. The predicted and experimental trends obtained by analyzing the effect of various operating parameters (light reflux flowrate, duration of feed/purge step, heavy product flowrate and mole fraction of heavy component in binary feed gas mixture) on process performance are also comparable. Overall, this simulation technique of dual-reflux pressure swing adsorption can serve as an effective tool for process design, cost reduction of laboratory and/or plant trails, and enhanced process understanding.

*Keywords:* Pressure swing adsorption; Dual-reflux; Mathematical modeling; Gas purification; Process simulation; Cyclic adsorption process

* Corresponding author. Tel.: +39 0223993154; Fax: +39 0223993180.

*E-mail:* renato.rota@polimi.it

https://doi.org/10.1016/j.ces.2014.09.013

## 1. Introduction

Since its inception more than half a century ago, the technology of pressure swing adsorption (PSA) has been widely studied and applied, becoming today the method of choice for the separation and/or purification of many gaseous mixtures. Some of its most popular industrial applications include hydrocarbon separation, hydrogen purification, air drying, and air separation. PSA systems employed for the processing of binary feed gas mixtures can be categorized into three main types: (i) stripping, (ii) rectifying and (iii) dual-reflux.

Stripping PSA systems are based on the Skarstrom cycle (Skarstrom, 1959) and are capable of producing only the light product (weakly adsorbed; in the following referred to as species $B$) at high purity, since the purity of the heavy product (strongly adsorbed; species $A$) is confined by thermodynamic constraints (Subramanian and Ritter, 1997). Rectifying PSA systems, developed by Diagne et al. (1994) and Ebner and Ritter (2002) and also known as enriching reflux PSA (Yoshida et al., 2003), have thermodynamic constraints on the purity of the light product, thus resulting in the capability of producing only the heavy product at high purities. In contrast, the purity of both the products is thermodynamically unconstrained in dual-reflux pressure swing adsorption (DR-PSA; Leavitt, 1992): consequently, DR-PSA processes are capable of achieving complete separation of binary feed gas mixture, thus producing two pure-component streams.

A typical DR-PSA unit comprises of a combined two-bed system with feed injection in a given position along the axis of the adsorption column. Such position ($Z_F$) divides each bed in two sections: '*Stripping Section*' ($SS$) and the '*Rectifying Section*' ($RS$). Two reflux streams (so the name DR-PSA), light reflux ($LR$, pure $B$), and heavy reflux ($HR$, pure $A$), are respectively injected at the $SS$ and $RS$ end of each column during constant pressure steps. Depending on the column operating pressure (high pressure, $P_H$, or low pressure, $P_L$) to which the binary feed gas mixture is supplied and the type of gas ($A$ or $B$) with which the pressure swing is carried out, four different cycle configurations can be identified (Kearns and Webley, 2006):

(i) DR-PL-A: Feed to $P_L$ and pressure swing with $A$;

https://doi.org/10.1016/j.ces.2014.09.013

(ii) DR-PL-B: Feed to $P_L$ and pressure swing with $B$;

(iii) DR-PH-A: Feed to $P_H$ and pressure swing with $A$;

(iv) DR-PH-B: Feed to $P_H$ and pressure swing with $B$.

Gas separation processes based on DR-PSA have been studied experimentally in the literature. Diagne et al. (1994, 1995a, 1995b) explored the application of this process to the $CO_2$ removal from air using zeolite 13X as adsorbent. In these studies they demonstrated that feed gas containing 20% $CO_2$ can be concentrated to values higher than 94% in the heavy product stream by proper selection of the operating conditions. More recently, McIntyre et al. (2010) conducted experiments using wood-based activated carbons in DR-PL-A configuration for the recovery and enrichment of dilute ethane from nitrogen. In this extensive study, they performed 19 runs for 1,500 to 3,000 cycles each and analyzed the effect of various operating parameters on process performance: light reflux flowrate, duration of feed/purge step, heavy product flowrate and feed mole fraction of the heavy component. It was demonstrated that the average of these 19 runs with an ethane feed concentration of 1.38 vol % gave an ethane enrichment of 45.8 times (63.2 vol %) and ethane recovery of 84%, while producing $N_2$ at high purity (99.8 vol %) and recovery (>99%). These experimental studies proved that both the light and heavy products can be obtained at high purities using DR-PSA systems.

Various modeling tools ranging from very simple to complex have been reported in the literature for the design and optimization of PSA units (cf. Ruthven et al., 1994; Spoorthi et al., 2011; Thakur et al., 2011; Sivakumar and Rao, 2011a, 2011b, 2012). The simplest modeling approach (usually indicated as Equilibrium Theory) involves a large set of simplifying assumptions, such as instantaneous linear equilibrium throughout the column, isothermal conditions, negligible mass transport resistances and axial mixing, negligible pressure drop, and ideal gas behavior. The resulting equations have been solved by the method of characteristics (Rhee et al., 1986) and its solution for conventional PSA systems was fully detailed by Knaebel and Hill (1985). Equilibrium Theory was applied to DR-PSA systems by Ebner and Ritter (2004), Kearns and Webley (2006) and most recently by Bhatt et al. (2013). At the opposite extreme, the detailed PSA modeling approach requires much less assumptions, thus considering nonlinear adsorption equilibrium along with transport limitations, pressure drop and temperature effects. Yang and Doong (1985)

https://doi.org/10.1016/j.ces.2014.09.013

were among the earliest to propose such a detailed modeling approach for conventional PSA systems and a similar approach has been used for DR-PSA by Diagne et al. (1996) and Thakur et al. (2011). Various configurations and/or process steps encountered in a PSA cycle need to be modeled via partial differential equations (PDEs) linked by the equation of state and the thermodynamic properties of the gas and adsorbed phases. Given the inherent complexity and iterative nature of PSA systems, the numerical solution of detailed models is computationally demanding and time consuming.

In this work, we present a detailed model for the simulation of DR-PL-A processes developed in the frame of the commercial software Aspen Adsim®. To validate the resulting model, all the 19 experimental runs reported by McIntyre et al. (2010) and considering the separation of the binary mixture nitrogen-ethane have been simulated. At cyclic steady-state, model predictions are compared with reported experimental results in terms of: (i) average ethane mole fraction in heavy product, (ii) average nitrogen mole fraction in light product, (iii) instantaneous heavy product composition profiles, and (iii) instantaneous column composition profiles. Simulation results and reported experimental trends obtained by analyzing the effect of various operating parameters (light reflux flowrate, duration of feed/purge step, heavy product flowrate and mole fraction of heavy component in binary feed gas mixture) on process performance are compared. For enhanced understanding of the process behavior, column composition profiles at the end of each process cycle step are also provided for every run at $CSS$. Finally, since the feed position was fixed in all the previous model calculations, additional simulations were performed to assess the effect of changing such position on process performance.

## 2. DR-PL-A cycle description

The schematic diagram of the twin-bed DR-PL-A system under consideration in this work is depicted in Fig. 1. In this particular configuration, each of the two adsorption beds ($Bed-I$ and $Bed-II$) undergoes a four step cyclic process: two steps are simultaneously executed at constant pressure and remaining two at non-constant pressure in both the beds. Note that only half-cycle is depicted in the figure, since the same steps occur with the column numbers transposed. The feed injection position along the bed, defined in terms of

https://doi.org/10.1016/j.ces.2014.09.013

normalized axial coordinate ($Z_F$), divides each column into two sections; it is a dimensionless value, $Z$ being the axial coordinate normalized with respect to the column length ($Z = z/L_{bed}$). The section to the left of the feed injection position ($Z < Z_F$) is termed as '*Stripping Section*' or $SS$ (material enriched in $B$ is either injected-in or pushed-out of the end of this section, $Z = 0$) and the section to the right of the feed injection position ($Z > Z_F$) is termed as '*Rectifying Section*' or $RS$ (material enriched in $A$ is either injected-in or pushed-out of the end of this section, $Z = 1$).

Binary feed gas mixture with flowrate $Q_F$ and composition $y_F$ (mole fraction of $A$ in feed gas mixture) is supplied to $Bed - I$ which is maintained at constant pressure equal to $P_L$ during the feed step ($FE$); simultaneously, $Bed - II$ undergoes purge step ($PU$) while being maintained at constant $P_H$. Material enriched in $A$ is pushed out of the $Bed - I$ undergoing $FE$ at flowrate $Q_{H,out}$. It is compressed and portion of $Q_{H,out}$ is taken out of the system as Heavy Product ($HP$) with flowrate $Q_{HP}$ and the remaining portion is supplied as Heavy Reflux ($HR$) to $Bed - II$ undergoing $PU$ at flowrate $Q_{HR}$. Material enriched in $B$ exits from $Bed - II$ at flowrate $Q_{L,out}$, a portion of which is taken out of the system as Light Product ($LP$) at flowrate $Q_{LP}$ and the remaining quantity is supplied as Light Reflux ($LR$) at flowrate $Q_{LR}$ to $Bed - I$. The average mole fractions of $A$ in light and heavy product are termed as $\bar{y}_{LP}$ and $\bar{y}_{HP}$ respectively. At the end of the simultaneous $FE/PU$, the bed pressures need to be interchanged. This is accomplished by transferring gas enriched in $A$ from the rectifying end ($Z = 1$) of $Bed - II$ (after compression) to the $Z = 1$ end of $Bed - I$. Hence $Bed - II$ undergoes blowdown step ($BD$) during which its pressure decreases from $P_H$ to $P_L$ and simultaneously $Bed - I$ undergoes pressurization step ($PR$) during which its pressure increases from $P_L$ to $P_H$. The total amounts (in kmol) of gas extracted from $Bed - II$ and transferred to $Bed - I$ during these steps are indicated as $N_{BD}$ and $N_{PR}$, respectively.

## 3. Model description and solution approach

As anticipated, the model aimed to the detailed simulation of the four-step DR-PL-A process described in section 2 was developed in the frame of the commercial software Aspen Adsim®. The process cycle is

https://doi.org/10.1016/j.ces.2014.09.013

simulated by applying the so-called 'Single Bed Approach', thus following the behavior of one single column out of the two beds working in parallel during the actual process. In order to reduce the computational effort while ensuring reliable simulation results, the following assumptions are considered in this work:

1. isothermal operation;
2. ideal gas behavior;
3. ideal plug-flow behavior without axial mixing;
4. lumped mass transport rates (constant mass transfer coefficient times a driving force in terms of concentrations in adsorbed phase);
5. non-linear adsorption isotherms expressed as a function of partial pressures through the 'Extended Langmuir' model;
6. pressure drop estimated via Ergun equation.

The model constitutive equations are fully detailed in Aspen Adsim® help menu; accordingly, they are omitted here, with the exception of some selected terms which are summarized below (the meanings of all variables and symbols used in this paper are provided in the final section Notations).

*Ideal gas behavior:*

$$Py_i = RTc_i \tag{1}$$

where, $P$ is the total pressure, $y_i$ is the bulk gas-phase mole fraction of component $i$, $R$ is the universal gas constant, $T$ is the system temperature and $c_i$ is the bulk gas-phase concentration of component $i$.

*Material balances:*

Material flow pattern through the adsorption column is assumed to be ideal plug-flow, without axial mixing. The mass balance for component $i$ over a differential volume element, accounting for convection as well as accumulation in both gas and solid phase is given by

$$\frac{\partial(v_g c_i)}{\partial z} + \varepsilon_T \frac{\partial c_i}{\partial t} + \rho_B \frac{\partial \bar{q}_i}{\partial t} = 0 \tag{2}$$

https://doi.org/10.1016/j.ces.2014.09.013

where, $v_g$ is the gas-phase superficial velocity, $z$ is the axial co-ordinate, $\varepsilon_T$ is the total bed voidage, $t$ is the time coordinate, $\rho_B$ is the adsorbent bulk density (i.e. the mass of the solid per unit volume of column) and $\bar{q}_i$ is the particle-average concentration of species $i$ in adsorbed phase per unit mass of solid.

*Mass transfer rate:*

The linear driving force (LDF) model was used to account for the resistances to mass transfer between the fluid and the porous media, given by

$$\frac{\partial \bar{q}_i}{\partial t} = k_{MTC_i}(q_i^* - \bar{q}_i) \tag{3}$$

where, $q_i^*$ is the adsorbent loading of component $i$ in equilibrium with the gas-phase composition and $k_{MTC}$ is the lumped, effective mass transfer coefficient ($MTC$). This parameter is calculated by assuming that only the resistances to mass transfer in the external fluid film and in the macropores are significant:

$$\frac{1}{k_{MTC_i}} = \frac{r_P \overline{K}_{K,i}}{3k_{f,i}} + \frac{{r_P}^2 \overline{K}_{K,i}}{15\varepsilon_P D_{P,i}} \tag{4}$$

where $r_P$ and $\varepsilon_P$ are the radius and porosity of the adsorbent particle ($P$), respectively. $\overline{K}_{K,i}$ is the local Henry's coefficient obtained from the equilibrium isotherm as:

$$\overline{K}_{K,i} = RT\frac{\rho_B}{\varepsilon_i}\frac{\partial q_i^*}{\partial p_i} \tag{5}$$

where, $\varepsilon_i$ is the interstitial (or external) porosity and $p$ represents the partial pressure. The macropore diffusion coefficient ($D_P$) is in turn computed from the following equation:

$${D_{P,i}}^{-1} = \tau\left({D_{K,i}}^{-1} + {D_{M,i}}^{-1}\right) \tag{6}$$

where, $\tau$ is the adsorbent tortuosity factor, $D_M$ is the constant molecular diffusion coefficient estimated by Aspen Adsim® properties database, and the Knudsen diffusion coefficient ($D_K$) is estimated using the following equation:

$$D_{K,i} = 97 r_{P,mac}\left(\frac{T}{M_{W,i}}\right)^{0.5} \tag{7}$$

where $r_{P,mac}$ is the macropore radius and $M_{W,i}$ is the molecular weight of the component. The film resistance coefficient $\left(k_{f,i}\right)$ is computed from the component Sherwood ($Sh_i$), Schmidt ($Sc_i$) and Reynolds ($Re$) number, using the following relationships:

https://doi.org/10.1016/j.ces.2014.09.013

$$Sc_i = \frac{\mu_g}{D_{M,i}\rho_g M_W} \quad (8)$$

$$Re = \frac{\left(2r_P M_W \rho_g v_g\right)}{\mu_g} \quad (9)$$

$$Sh_i = 2 + 1.1{Sc_i}^{1/3}{Re_i}^{0.6} \quad (10)$$

$$k_{f,i} = \frac{\left(Sh_i D_{M,i}\right)}{2r_P} \quad (11)$$

where, $\mu_g$ is the dynamic gas viscosity and $\rho_g$ is the molar gas-phase density.

*Momentum balance:*

Pressure drop along the axial coordinate (valid for both laminar and turbulent flows) is estimated by Ergun's equation (Ergun, 1952). Pressure drop estimates depend on the flow direction of the bulk gas during different steps of the process cycle. Accordingly, the $(\partial P/\partial z)$ estimate of Eq. (12) should be considered to be negative during: Blowdown ($BD$) and Feed ($FE$); and positive during Pressurization ($PR$) and Purge ($PU$) steps.

$$\frac{\partial P}{\partial z} = \pm\left[\mu v_g \frac{0.15(1-\varepsilon_i)^2}{(2r_P\psi)^2{\varepsilon_i}^3} + 1.75\times 10^{-3} M_W \rho_g {v_g}^2 \frac{(1-\varepsilon_i)}{2r_P\psi{\varepsilon_i}^3}\right] \quad (12)$$

where $\psi$ is the shape factor of the adsorbent particles.

*Equilibrium isotherm:*

The adsorption isotherm of the gaseous mixture is predicted from pure component isotherms by the so-called Extended Langmuir model. Namely, the adsorbed moles of component *i* per unit mass of adsorbent at equilibrium $(q_i^*)$ are given by:

$$q_i^* = \left[\left(IP_{1,i}\right)\left(p_i\right)\right] \Big/ \left[1 + \sum_{k=1}^{2}\left(IP_{2,k}\right)\left(p_k\right)\right] \quad (13)$$

https://doi.org/10.1016/j.ces.2014.09.013

where $IP_{1,i}$ and $IP_{2,i}$ are the Langmuir isotherm parameters for the pure component $i$ and $p$ represents the gas partial pressure.

A qualitative representation of the considered DR-PL-A process simulation flowsheet is shown in Fig. 2. As anticipated, the process cycle is simulated by applying the so-called 'Single Bed Approach' until the achievement of cyclic steady-state conditions ($CSS$). The evolution of concentration, pressure and velocity profiles in the simulated column is followed step by step throughout the duration of the entire separation cycle, whereas the interplay with the second bed is accounted for through the introduction of 'interaction modules' ($I$): this way, all the properties of the selected leaving stream are recorded and then reproduced as input stream (as a first-in-first-out buffer profile) when required in the frame of the process cycle. As per the description of twin-bed DR-PL-A system elucidated in section 2, both the adsorbent beds undergo the same steps in a given cycle and are assumed to be identical (i.e., with same length, feed position, cross-sectional area ($A_{bed}$), kind and amount of adsorbent, particle size, interstitial porosity ($\varepsilon_i$), particle porosity ($\varepsilon_P$), solid ($\rho_S$) and bulk densities ($\rho_B$)). The selected computational scheme, based on the simulation of the complete cycle of one single bed, significantly improves the computational speed since it reduces the total number of equations to be solved for achieving the final results. Moreover, the 'Single Bed Approach' retains the accuracy of multiple bed simulation provided the transfer of information through the previously mentioned interaction modules is accurate enough.

In accordance with the twin-bed DR-PL-A system depicted in Fig. 1, the simulated single column is sketched in Fig. 2 as a series of two fixed-beds, Stripping Section ($SS$) and Rectifying Section ($RS$). The respective lengths of these two sections define the position of the feed injection ($Z_F$) with respect to the whole column. Since a single gas stream can enter or leave a fixed bed in Aspen Adsim®, the input and output streams of $RS$ and $SS$ are connected to the so-called 'gas tank void' modules. These tanks are set to be of negligible volume and serve as connectors for multiple streams entering and exiting the beds. Specifically, the tank connected to the $SS$ end ($Z = 0$) is termed as '$SS$ Tank', the one connected to the $RS$ end ($Z = 1$) '$RS$ Tank' and the one in-between the two beds 'Feed Tank'.

https://doi.org/10.1016/j.ces.2014.09.013

The flowrates ($Q$) of light reflux ($LR$), feed ($F$), heavy reflux ($HR$), blowdown ($BD$), heavy product ($HP$) and light product ($LP$) are respectively regulated through the valves $V_{LR}$, $V_F$, $V_{HR}$, $V_{BD}$, $V_{HP}$ and $V_{LP}$. The extent of opening (or simply the position) of all of these valves can be set as required by the specific step scenario. When open, all these valves ensure a specified flowrate with the exception of $V_{LP}$ and $V_{HR}$, whose flowrate is governed by PID controllers. The controller that governs $Q_{LP}$ via $V_{LP}$ is termed as light product flowrate controller ($LPFC$) and the one that governs $Q_{HR}$ via $V_{HR}$ is termed as heavy reflux flowrate controller ($HRFC$). Since light product is released during $PU$ and heavy reflux is released during $FE$, the $P_H$ and $P_L$ set points (input quantities) are respectively maintained by $LPFC$ and $HRFC$ by flowrate manipulation of the specific streams.

The solution sequence of the module is governed by the 'Cycle Organizer' which allows to create the steps and to manage all the variables and the working conditions that occur in the cyclic process. Inside such organizer it is possible to create any number of steps, define the step termination event (like the duration of a constant pressure step or the end pressure of a variable pressure step) and manipulate the flowsheet variables for a given step (such as the closing of the valves, opening of the valves at a specific flowrate, etc.). Furthermore, the 'Cycle Organizer' allows handling all the interaction modules which appear in the flowsheet making possible the simulation of the entire cycle.

## 4. Model adaptation to experimental apparatus and procedures

As already mentioned, model validation is carried out by simulating the experimental data by McIntyre et al. (2010). Namely, 19 experiments in DR-PL-A configuration for the recovery and enrichment of dilute ethane ($C_2H_6$) in nitrogen ($N_2$) using MeadWestvaco BAX-1500® activated carbon have been considered. The pure component adsorption isotherms of $C_2H_6$ and $N_2$ on the selected activated carbon were provided by McIntyre et al. (2002). In the operating range of the experiments, $C_2H_6$ is adsorbed more than $N_2$:

https://doi.org/10.1016/j.ces.2014.09.013

accordingly, $C_2H_6$ is henceforth referred to as heavy component ($A$) and $y_F$ refers to its mole fraction in the binary feed gas mixture.

Model parameter values, kept constant while simulating all the runs, are listed in Table 1, whereas the values of the operating parameters that varied during the simulation of individual runs are listed in Table 2. To maintain consistency, the simulated Run numbers used in this work are identical to the ones used by McIntyre et al. (2010); hence, Table 2 in this work is identical to Table 2 in the paper by McIntyre et al. (2010).

About the values in Table 1, length and diameter of each column ($SS$ and $RS$) were set according to the description of the experimental apparatus provided by McIntyre et al., 2010. The amount of adsorbent ($M_{ads}$) in each of the columns was also stated, thus allowing the evaluation of the adsorbent bed volume ($V_{bed}$) and bulk density ($\rho_B$). The values of average length and radius of adsorbent pellets mentioned by Tolles et al. (2009) were utilized to calculate the radius ($r_P$) of equivalent spherical particles ($\psi = 1$). Mesoporous as well as macroporous volume ($V_{meso+macro}$) along with maximum macropore radius ($r_{P,mac}$) of the adsorbent, mentioned by Wilhelm et al. (2005) were assumed. The average tortuosity ($\tau$) value mentioned by Ruthven et al. (1994) for activated carbons was utilized in the model calculations. The interstitial (or external) porosity ($\varepsilon_i$) provided by Hou et al. (2010) was assumed. This estimated value of $\varepsilon_i$ also matches the overall bulk porosity range for densely packed beds with cylindrical pellets, mentioned by Zhang et al., 2006. This information was utilized to estimate the value of the adsorbent particle porosity ($\varepsilon_P$) as follows:

$$\varepsilon_P = \frac{M_{ads}(V_{meso+macro})}{V_{bed}(1-\varepsilon_i)} = \frac{\rho_B(V_{meso+macro})}{(1-\varepsilon_i)} \tag{14}$$

The experimental apparatus was using a pump for pressurization and depressurization. Instead of using a pump module in the simulation (which parameters were not provided in the corresponding paper), the values

https://doi.org/10.1016/j.ces.2014.09.013

of all the molar flowrates were input for any given step, and the material flow direction was governed by setting the following information in the cycle organizer:

(i) pressure values of the corresponding module at the entry/exit point of the streams;

(ii) close (✗) or open (✓) valves at designated and/ or controlled flowrates and;

(iii) whether an interaction module is nonfunctional (✗) or recording information ($\mathbb{R}$) or feeding back the recorded information ($\mathbb{F}$).

The specific implementation of these input values for each experimental run will be detailed in the following section (cf. Table 3).

The $P_H$ and $P_L$ set points (Table 1) used in $LPFC$ and $HRFC$, respectively, have been kept constant for all simulations and identical to the approximate values provided by McIntyre et al. (2010) for all experimental runs. In the same paper, only the durations of $PR$ and $BD$ steps (10 seconds for all the runs) were provided without the mention of the total amount of material pushed out of one column during $BD$ and then supplied to the second column during $PR$, thus preventing the evaluation of the actual profile (or time evolution) of flowrate. However, the complete pressure profile of both the columns was provided for the base case (Run # 1) and it was mentioned that the pressure profile for all other runs is similar. Based on this analogy, the average pressure at the end of the $BD$ step of both the columns was assumed equal to the value $P_{BD,end}$ in Table 1. Therefore, a specific value of the depressurization flowrate $Q_{BD}$ being pushed out of the column during step $BD$ was evaluated in order to reduce the column pressure down to $P_{BD,end}$ at the end of the step. The resulting value (cf. Table 1) was recorded in $RS$ Tank (event driven step) and the amount of material accumulated during $BD$ was then supplied back to the column during $PR$. This arrangement slightly increased the cycle time but provided a reasonable reproduction of the experimental pressure profiles.

According to McIntyre et al. (2010), the first experimental run (Run # 1, the base case) was initiated with the columns filled with pure $N_2$. After $CSS$ was achieved, a process condition was changed, and a new run commenced from the periodic state of the previous run; this same approach was applied to the complete series of experiments. Accordingly, the same procedure was applied in modeling: the simulation of Run # 1 was initiated using pure $N_2$ in all the bed, tank and interaction modules, while all simulation runs thereafter

https://doi.org/10.1016/j.ces.2014.09.013

were initiated using the concentration profiles predicted for the previous run at $CSS$ following the same order of the 19 experimental runs reported by McIntyre et al. (2010).

As mentioned in the original paper, temperature oscillations of around 25 K were observed for all the reported experimental runs. This temperature variation is lower than those typical of conventional PSA systems and is explained by the limited pressure ratio $P_H/P_L$ along with the low concentration of the most adsorbable component in the feed, less than 1.4% on molar basis. Accordingly, the simulations were carried out at constant temperature equal to 298 K, using model parameter values estimated at the same temperature.

All 19 simulations were carried out for batch intervals of 1,500 cycles. In order to assess the actual achievement of $CSS$ conditions, once the time invariance of the cycle-average compositions was reached the component material balances were checked after every batch and steady-state conditions were considered to be established when the resulting error was less than 5% for $C_2H_6$ and less than 2% for $N_2$, similar to the criterion mentioned by McIntyre et al. (2010). At $CSS$, the average $N_2$ material balance error for all the runs was about 0.03% whereas the same assessment for $C_2H_6$ was about 2.5%. The larger error in $C_2H_6$ material balance was due to the very low concentration of $C_2H_6$ in the feed stream. If $CSS$ was not established, a further batch of 1,500 simulation cycles was carried out and the checking procedure was repeated. Usually $CSS$ was achieved sooner than anticipated in most of the simulations (say, around 800 cycles); however, we decided to run the same number of cycles as reported by the experimenters to maintain consistency and also to check the $CSS$ robustness. Depending on the cycle duration, the overall computational time ranged from 3 days to 2 weeks on Intel® Xenon® X5650, 2.66GHz, 64-bit processor.

## 5. Base case simulation

This section provides a detailed description of the approach used for simulating Run # 1 (base case); the same approach was used for simulating all other runs. As anticipated, all the parameter values stated in Table 1 were used. A four step DR-PL-A cycle was formulated in the cycle organizer ($BD$, $FE$, $PR$ and $PU$). The simulation of $BD$ step was executed until the desired pressure value $P_{BD,end}$ was recorded in $RS$ Tank

https://doi.org/10.1016/j.ces.2014.09.013

(event driven step), whereas $FE$ was executed for the time stated in Table 2 (time driven step). Of course, the execution times of the parallel steps $PR$ and $PU$ were equivalent to that of $BD$ and $FE$, respectively. Once the execution methodology of these four steps was defined, the *modus operandi* of the various valves and interaction modules during each step in the cycle organizer was defined as shown in Table 3.

The cycle starts with blowdown ($BD$) step and the column is depressurized from $P_H$ to $P_{BD,end}$. The gas mixture is withdrawn from $Z = 1$ end of the column at $Q_{BD}$ (cf. Table 1) via $V_{BD}$ and the evolutions of concentration, pressure and flow profiles are recorded in the pressure interaction module ($PI$). Then, the feed step ($FE$) is simulated for the time $t_{FE}$ mentioned in Table 2. Light reflux material is fed to the column at constant flowrate $Q_{LR}$ (Table 2) via the light reflux interaction module ($LRI$); simultaneously, the binary feed gas mixture with composition $y_F$ (Table 2) is fed to the column at fixed flowrate $Q_F$ (Table 2) via $V_F$. Material withdrawn from $Z = 1$ end of the column during this step is divided into two streams and gets collected by: (i) heavy product module at constant flowrate ($Q_{HP}$ in Table 2) via $V_{HP}$ and (ii) heavy reflux interaction module ($HRI$) at flowrate $Q_{HR}$ controlled by $HRFC$ via $V_{HR}$ in order to maintain the outlet pressure equal to the set point $P_L$ (Table 1). Note that the material withdrawn from $Z = 1$ end of the column during this step is flowing to the Heavy Product module as first priority (by default simulation settings), while the remaining material is sent to $HRI$. This way, the heavy product flowrate (set equivalent to the corresponding experimental value) is consistently maintained in the simulation. Next, the pressurization step ($PR$) is simulated. Pressure interaction module ($PI$) feeds back a stream with the profiles recorded during $BD$ at the flowrate $Q_{PR}$ (equivalent to $Q_{BD}$).

At the high pressures resulting from $PR$, the purge step ($PU$) is executed. The heavy reflux ($Q_{HR}$) is pushed by $HRI$ (recorded during $FE$) inside the column. Material withdrawn from $Z = 0$ end of the column during this step is divided into two streams and gets collected by: (i) Light product module at flowrate $Q_{LP}$ controlled by $LPFC$ via $V_{LP}$ in order to maintain the pressure at the set point $P_H$ (Table 1) and (ii) Light reflux interaction module ($LRI$) at constant flowrate ($Q_{LR}$ in Table 2) via $V_{LR}$. Similar to step $FE$, in order to assure light reflux flowrate equal to the experimental one, the material withdrawn from $Z = 0$ end of the

https://doi.org/10.1016/j.ces.2014.09.013

column during this step is flowing to $LRI$ with first priority (by default simulation settings) and then the remaining material is sent to the light product module.

Once established $CSS$ conditions, model predictions were compared with reported experimental results in terms of: (i) average $C_2H_6$ mole fraction in heavy product ($\bar{y}_{HP}$); (ii) average mole fraction of $N_2$ in light product ($1-\bar{y}_{LP}$); (iii) instantaneous heavy product composition ($y_{HP}$: $C_2H_6$ mole fraction in heavy product) profiles during $FE$ step and; (iii) instantaneous column composition profiles (in terms of $C_2H_6$ mole fraction: $y_{C_2H_6}$) at the end of $PU$ step.

Pressure profile and flow pattern of various streams during one cycle at $CSS$ are depicted in Fig. 3a) and 3b), respectively. The model estimated blowdown and pressurization times are normalized with respect to the one reported by McIntyre et al. (2010). The cycle time ($t_{cycle}$) is identical for both figures: 3a) and 3b). Since negligible pressure drop was observed across the simulated column length, the pressure profile of $SS$ Tank is representative of the entire column. For comparative analysis, actual experimental pressure profile of both the columns (reported in their Fig. 3 by McIntyre et al., 2010; measured near $Z=0$ end of each column) is also plotted in the same figure. Note that the pressure profiles during a complete cycle ($BD$, $FE$, $PR$ and $PU$) occurring in *each* of the experimental columns are plotted in Fig. 3a). Discrepancy between the experimental and simulation pressure profile can be ascribed to the simplistic model assumptions coupled with the fact that the pump module was not utilized in the simulation. In general, the experimental and calculated pressure profiles are comparable and the close achievement of $P_L$ and $P_H$ set points (Table 1) is apparent from Fig. 3a). As explained above, $Q_{HR}$ is the variable manipulated by $HRFC$ (via $V_{HR}$) to ensure pressure equal to $P_L$ during the feed step: since the step starts at $P_{BD,end}$ (which is higher than the set point, $P_{BD,end} > P_L$), valve $V_{HR}$ is fully open and the corresponding flow (heavy reflux) reaches its maximum limit (the bias of $HRFC$) and remains equal to such value until the set point pressure is established at $RS$ Tank. Conversely, $PU$ starts at a pressure value lower than the set point $P_H$: therefore, $LPFC$ restricts $Q_{LP}$ by closing the valve $V_{LP}$ until the set point pressure is established at $SS$ Tank and then manipulates the same

https://doi.org/10.1016/j.ces.2014.09.013

flow to maintain the pressure constant and equal to $P_H$. Note that this second interval corresponds to non-zero and non-constant $Q_{LP}$ in Fig. 3b).

While simulating all the available experimental runs, a reasonable match between simulation and experimental results at $CSS$ could be obtained when a pressure profile very similar to the one shown in Fig. 3a) was qualitatively established. As explained above, the pressure profile was mainly determined by fine-tuning both the controllers, $HRFC$ and $LPFC$. Moreover, after establishing $CSS$ conditions, the consistency between experimental and simulation results was checked by mass balance calculations, as elaborated in the next section.

## 6. Results and discussion

In this section, a comparative analysis between simulation and reported experimental results at $CSS$ is presented for all the available experimental conditions. Namely, the effect on process performance of the following process parameters is explored:

a) light reflux flowrate $(Q_{LR})$: Run # 1 to 6;

b) feed or purge step time $\left(t_{FE/PU}\right)$: Run # 7, 8, 1 and 9 to 12;

c) heavy product flowrate $(Q_{HP})$: Run # 13, 1, 14 and 15;

d) ethane mole fraction $(y_F)$ in binary feed gas mixture: Run # 16, 17, 1, 18 and 19.

In order to maintain consistency, the maximum and minimum limits of both the axes for each case are held constant for ease of comparison. In all cases, 1,500 to 3,000 cycles were simulated to achieve $CSS$: besides being identical to the typical experimental values, the cyclic steady state nature of the simulation results was demonstrated by fulfilling the following constraints:

(i) material balance error of the component, less than 5% for $C_2H_6$ and 0.1% for $N_2$ (values respectively identical and much more stringent than those reported by the experimenters);

https://doi.org/10.1016/j.ces.2014.09.013

(ii) achievement of both experimental set point values of pressure, $P_H$ and $P_L$;

(iii) pressure profile and flow pattern of various streams qualitatively similar to those shown in Fig. 3 for the base case and;

(iv) bed composition profile at the end of $PU$ and the composition profile of heavy product during $FE$ for each run were very similar to the ones reported by McIntyre et al., 2010.

The experimental flowrates $Q_F$, $Q_{HP}$, $Q_{LR}$ (cf. Table 2) and the pressure values $P_H$, $P_L$ (cf. Table 1) were set and/or maintained in all simulations. On the other hand, the flowrate $Q_{LP}$ was not fixed in the experimental setup, but controlled in the model simulations by $LPFC$ via $V_{LP}$ in order to maintain the set point pressure $P_H$. Regardless of this dissimilarity, a very good match was found between the light product flowrate ($Q_{LP}$) recorded in the experiments and predicted by the model in all examined cases. This agreement represents a meaningful model validation in terms of the remaining flowrate $Q_{HR}$ and of the internal recycle loop. Simulated values of heavy reflux flowrates ($Q_{HR}$) as a function of operating parameters are also presented. Since the specific values of $Q_{HR}$ were not mentioned by McIntyre et al. (2010), simulated data is not compared with experimental results for this specific parameter. Moreover, for enhanced understanding of the process behavior, column composition profiles (in terms of $C_2H_6$ mole fraction: $y_{C_2H_6}$) at the end of each process cycle step are also provided for every run at $CSS$.

**Effect of the light reflux flowrate ($Q_{LR}$): Run # 1 to 6**

Following the procedure described in the previous section, Runs # 1 to 6 were simulated to assess the effect of changing the light reflux flowrate ($Q_{LR}$) on process performance when keeping constant all the remaining conditions (cf. Table 2). The values of the operating parameters used while simulating these runs are shown in the same table, whereas the simulation results are plotted and compared with the experimental ones in Fig. 4 and 5.

$Q_F$ and $Q_{HP}$ were kept practically constant as $Q_{LR}$ was increased from Run # 1 to 6. Since practically constant $Q_{LP}$ was also observed in these runs, the only obvious flowrate being manipulated by the system is

https://doi.org/10.1016/j.ces.2014.09.013

$Q_{HR}$, as depicted in Fig. 4c) and also indicated by McIntyre et al. (2010). Therefore, $Q_{HR}$ increased with increase in $Q_{LR}$ that, in turn, caused an increase in the flowrates of the internal recycle loop.

In agreement with the remarks reported by McIntyre et al. (2010), two competing effects come into play in this case: (i) improved bed regeneration during $FE$ due to the increase in $Q_{LR}$ (manifested by the column composition profiles at the beginning and end of $FE$ in Fig. 6) and (ii) deeper $C_2H_6$ penetration into the column due to the increase in $Q_{HR}$ (evident from Fig. 5c and 5d). At lower $Q_{LR}$ values, the first effect is dominant, thus causing an increase in $\bar{y}_{HP}$ (Fig. 4a) and $(1-\bar{y}_{LP})$ (Fig. 4b). On the contrary, $C_2H_6$ penetration into the column (Fig. 5c and 5d) becomes dominant at higher $Q_{LR}$ values, resulting in decline of $\bar{y}_{HP}$. The initial increment in $Q_{LR}$ results in an increase in light product purity $(1-\bar{y}_{\mathrm{LP}})$, however, such parameter practically remains unaffected by further increment in $Q_{LR}$ values. These practically constant light product purities imply that the deeper $C_2H_6$ penetration into the column due to the increase in $Q_{HR}$ was not enough to significantly affect the column composition profiles at $Z = 0$ end (depicted in Fig. 6). It is also evident from Fig. 6 that the increase in internal recycle loop (due to increase in both $Q_{LR}$ and $Q_{HR}$) from Run # 1 to 6 increases the volume of adsorbent involved in the actual adsorption and desorption process. This combination of effects, result in the trends depicted in Fig. 4a), 4b) and, 5, in good agreement with the experimental observations.

The dip in some of the column composition profiles (in terms of $C_2H_6$ mole fraction: $y_{C_2H_6}$) at the *end* of high pressure $PU$ step *beyond* the feed position $(Z = 0.5)$ reported by the experimenters (depicted in Fig. 5c and some other runs, to be investigated later on) are noteworthy. McIntyre et al. (2010) reported that such perturbations result from the mixing of dilute ethane feed stream with an ethane rich gas inside the column during the low pressure feed step $(FE)$. The simulation results also show such perturbations at the *end* of $FE$ (as depicted in Fig. 6) at the feed position. As the cycle proceeds, the experimenters report that such perturbations appeared in the column composition profiles (for some of the runs) at the *end* of the $PU$ step *beyond* the feed position $(Z = 0.5)$, while in the simulations such perturbations were only observed specifically at the feed position. The model behavior seems more physically consistent: considering that during *PR* and *PU* steps the flow is reversed (that is, from $Z$ = 1 towards $Z$ = 0), the perturbation is expected

https://doi.org/10.1016/j.ces.2014.09.013

to move towards $Z$ = 0, that is, it should either appear also *before* and not only *beyond* the feed position $(Z = 0.5)$ or be reabsorbed.

**Effect of the feed/purge step duration $(t_{FE/PU})$: Run # 7, 8, 1 and 9 to 12**

Simulations for Run # 7, 8, 1 and 9 to 12 were performed to assess the effect of increasing feed/purge step duration $(t_{FE/PU})$ on process performance. Again, all the remaining model parameters remained practically constant (cf. Table 2), whereas the simulation results are compared to the experimental ones in Fig. 7 and 8. Column composition profiles at the end of each process cycle step are provided for every run at $CSS$ in Fig. 9.

According to McIntyre et al. (2010), the increase in $t_{FE/PU}$ had minimal effect on $C_2H_6$ uptake by the adsorbent due to the very low concentration of $C_2H_6$ in the feed. However, heavy and light recycle flowrates were allowed to persist longer with increasing duration of the feed/purge step (evident in Fig. 9 by the increases in the volume of adsorbent involved in the actual adsorption and desorption process with increase in $t_{FE/PU}$): this might explain the initial surge in $\bar{y}_{HP}$ and $(1 - \bar{y}_{LP})$ with increase in $t_{FE/PU}$. After this initial increase, the two competitive effects of bed regeneration (due to increase in light recycle time: evident from the column composition profiles at the beginning and end of $FE$ depicted in Fig. 9) and $C_2H_6$ penetration in the column (due to increase in heavy recycle time: evident from Fig. 8c and 8d and the column composition profiles at the beginning and end of $PU$ depicted in Fig. 9) cancel each other, resulting in the stable trends observed in Fig. 7a) and 7b).

Notice that the increments in $t_{FE/PU}$ resulted in decline of $Q_{HR}$ (Fig. 7c). In the original paper, it was mentioned that the pressure profile for all the runs was similar to the one provided for the base case (Run # 1); the simulation results confirmed this expectation. Table 2 shows that all operating parameters remained nearly constant as $t_{FE/PU}$ increased from Run # 7, 8, 1 and 9 to 12. Therefore, when increasing $t_{FE/PU}$ in these runs: the system managed to attain and maintain the designated pressure set points by decreasing $Q_{HR}$.

https://doi.org/10.1016/j.ces.2014.09.013

The unusual column composition profiles for Run # 7 (depicted in Fig. 9a) are noteworthy, since only in this run the heavy component concentration in $Z$ = 1 at the *FE* start is lower than that at the *FE* end. In this run, the short duration of low pressure $FE$ (desorption step: since the pressure reduces from $P_{BD,end}$ to $P_L$, cf. Table 1) did not allow for enough heavy product withdrawal from the bed. This phenomenon can be further verified from the instantaneous heavy product composition profile during $FE$ (depicted in Fig. 8a and 8b). On the other hand, the short duration of the high pressure $PU$ (adsorption step, where the pressure still increases, cf. Fig. 3) was not enough to adsorb the incoming ethane rich heavy reflux. These combined effects led to the unusual column composition profiles for Run # 7.

**Effect of the heavy product flowrate ($Q_{HP}$): Run # 13, 1, 14 and 15**

Simulations for Run # 13, 1, 14 and 15 were performed to assess the effect of increasing the heavy product flowrate ($Q_{HP}$) on process performance. The simulation results are plotted and compared with the experimental ones in Fig. 10 and 11 whereas, column composition profiles at the end of each process cycle step are depicted for every run at $CSS$ in Fig. 12. In these runs, $Q_{LR}$ holds identical values and the process is always able to attain the same $P_H$ and $P_L$ set points (Table 1). Since other operating parameters practically remained constant during these runs (Table 2), the decline of $Q_{HR}$ with increase in $Q_{HP}$ is apparent from Fig. 10c. This $Q_{HR}$ trend is in agreement with the experimental observations leading to reduced $C_2H_6$ penetration in the column (Fig. 11c and 11d) that, in turn, caused declining $\bar{y}_{HP}$ trend (Fig. 10a) and rising $(1-\bar{y}_{LP})$ trend (Fig. 10b). Reduced $Q_{HR}$ also lowers the volume of adsorbent involved in the major adsorption and desorption activity (as depicted in Fig. 12). The experimental and predicted heavy product composition profile trends (depicted in Fig. 11a and 11b) are also in agreement with one another.

**Effect of ethane mole fraction ($y_F$) in the feed mixture: Run # 16, 17, 1, 18 and 19**

Simulations for Run # 16, 17, 1, 18 and 19 were performed to assess the effect of change in ethane mole fraction ($y_F$) in the binary feed gas mixture on process performance. The simulation results are compared

https://doi.org/10.1016/j.ces.2014.09.013

with those reported by McIntyre et al. (2010) in Fig. 13 and 14. Column composition profiles at the end of each process cycle step are provided for every run at $CSS$ in Fig. 15. The parameters remaining practically constant in these runs are: $Q_F$, $Q_{HP}$, $Q_{LR}$ and $t_{FE/PU}$ (Table 2). Increase in $y_F$ resulted in an increased $C_2H_6$ (heavy component or strongly adsorbed species) uptake by the adsorbent. In this scenario, the system managed to attain the same $P_L$ set point (Table 1) by increasing $Q_{HR}$ (Fig. 13c). This combined effect of increased $C_2H_6$ uptake and deeper $C_2H_6$ penetration in the column (due to increase in $Q_{HR}$: evident from Fig. 14c and 14d) lead to an increase in heavy product purity (Fig. 13a) and decrease in light product purity (Fig. 13b). The experimental and predicted instantaneous heavy product composition profile trends (depicted in Fig. 14a and 14b) are also in agreement with one another. It can be observed that the volume of adsorbent involved in the actual adsorption and desorption process increases with increase in $y_F$.

**Effect of dimensionless feed position ($Z_F$)**

In all the 19 runs reported by McIntyre et al. (2010), the dimensionless feed position was fixed ($Z_F = 0.5$). Once the model was validated by comparative analysis of simulation and experimental results at $CSS$, additional simulations were performed to assess the effect of change in the dimensionless feed position ($Z_F$) on process performance. The results of these simulations are presented in Fig. 16, 17 and 18. Note that, except $Z_F$, the values of all other operating parameters were identical to those of the base case (Run #1). Since the total bed length ($L_{bed}$) was also held constant, by changing the dimensionless feed position we actually change the lengths of the column sections. Such changes impact on the process performance in non-trivial way, as explained below.

Notably, process performance remains unaffected for $Z_F \leq 0.5$. This can be clearly understood by examining the base case column composition profile reported by McIntyre et al. (2010) at the end of high pressure purge ($PU$) step: it is nearly equal to the feed gas composition for $Z \leq 0.4$. According to the DR-PL-A cycle description mentioned in section 2, after $PU$ the bed is depressurized ($BD$) by removing gas from the rectifying end ($Z = 1$), and then the feed step ($FE$) starts. The base case simulation revealed that the constant composition plateau at $y_F$ moves further right (towards $Z = 1$ end) during $BD$ and extends till

https://doi.org/10.1016/j.ces.2014.09.013

$Z \cong 0.5$ at the start of $FE$ (Fig. 18c). Since ethane concentration in the feed and column do not differ significantly till this dimensionless position in the column, the process performance remains unaffected for $Z_F \leq 0.5$. This can be clearly understood by examining the instantaneous heavy product composition profiles (Fig. 17a) and column composition profiles (Fig. 17b and 18a, 18b, 18c and 18d) for $Z_F \leq 0.5$.

The picture changes when $Z_F$ value beyond 0.5 is considered: $N_2$ concentration in the rectifying section ($RS$) increases (as evident from Fig. 17b, and 18e). Nitrogen, being the light component, desorbs much quickly than ethane: then, the time required by the system to attain the low pressure ($P_L$) set point (during $FE$) reduces. Once $P_L$ is achieved by the system, $HRFC$ closes $V_{HR}$ (thereby ceasing $Q_{HR}$). Hence, although $Q_F$, $Q_{HP}$ and $Q_{LR}$ (equivalent to Run # 1) are constant, the decrease in $Q_{HR}$ (Fig. 16c) hampers the internal recycle loop for $Z_F$ value beyond 0.5. This causes the decline of $\bar{y}_{HP}$ and $(1 - \bar{y}_{LP})$ depicted in Fig. 16a) and 16b), respectively.

## 7. Conclusions

A model developed in the frame of the commercial software Aspen Adsim® for the detailed simulation of dual-reflux pressure swing adsorption process (DR-PSA) is presented. Model intricacies needed for the detailed simulation of DR-PSA process are also elaborated. Even though the model can be readily applied for simulating different DR-PSA configurations, we focused exclusively on DR-PL-A configuration (feed to $P_L$ and pressure swing with $A$). Simulations were performed after model adaptation to the experimental apparatus and procedures reported by McIntyre et al. (2010) for recovery and enrichment of dilute ethane from nitrogen. Detailed description of the approach used for simulating a reference case (the so-called base case, Run # 1) is provided.

In accordance with the reported experimental modus operandi, 19 simulations were performed to analyze the effects of different operating parameters on process performance: (i) light reflux flowrate ($Q_{LR}$); (ii) feed or purge step time $(t_{FE/PU})$; (iii) heavy product flowrate ($Q_{HP}$) and (iv) ethane mole fraction ($y_F$) in the feed mixture. At $CSS$, model predictions were found to be in good agreement with reported experimental results

https://doi.org/10.1016/j.ces.2014.09.013

602 in terms of: (i) average $C_2H_6$ mole fraction in heavy product ($\bar{y}_{HP}$) and; (ii) average nitrogen mole fraction
603 in light product ($1 - \bar{y}_{LP}$). Pressure profile, $C_2H_6$ mole fraction profile in the heavy product during $FE$ and
604 $C_2H_6$ mole fraction profile in the column at the end of $PU$ were also found to be qualitatively similar to the
605 experimental ones. For enhanced understanding of the process behavior, column composition profiles at the
606 end of each process cycle step are also provided for every run at $CSS$. Finally, since the feed position was
607 fixed in all the 19 runs reported by McIntyre et al. (2010), additional simulations were performed to assess
608 the effect of change in feed position on process performance.
609
610
611 Overall, the model exhibited reliability and versatility (it can be applied to different unit arrangements as
612 well as DR-PSA process configurations) thereby serving as an effective tool for process design, cost
613 diminution of laboratory and/or plant trails, and enhanced process understanding.
614
615
616

https://doi.org/10.1016/j.ces.2014.09.013

## Notations

| | |
|---|---|
| $A$ | strongly adsorbed species, heavy product/ component |
| $A_{bed}$ | cross-sectional area of the adsorption column, $m^2$ |
| $B$ | weakly adsorbed species, light product/ component |
| $BD$ | Blowdown step |
| $Bed-I$ | Adsorption column depicted in Fig.1 |
| $Bed-II$ | Adsorption column depicted in Fig.1 |
| $c_i$ | Bulk gas-phase concentration of component $i$, $kmol/m^3$ |
| $CSS$ | Cyclic steady state |
| $D_{column}$ | Diameter of each adsorption column, $m$ |
| $D_K$ | Knudsen diffusion coefficient, $m^2/s$ |
| $D_M$ | Molecular diffusion coefficient, $m^2/s$ |
| $D_P$ | Macropore diffusion coefficient, $m^2/s$ |
| DR-PH-A | dual-reflux pressure swing adsorption system with feed to high pressure bed and pressure swing using heavy gas |
| DR-PH-B | dual-reflux pressure swing adsorption system with feed to high pressure bed and pressure swing using light gas |
| DR-PL-A | dual-reflux pressure swing adsorption system with feed to low pressure bed and pressure swing using heavy gas |
| DR-PL-B | dual-reflux pressure swing adsorption system with feed to low pressure bed and pressure swing using light gas |
| DR-PSA | dual-reflux pressure swing adsorption |
| $\mathbb{F}$ | represents that the interaction module is feeding back the recorded information |
| $FE$ | Feed step |
| $HP$ | Heavy product |
| $HR$ | Heavy reflux |
| $HRFC$ | Heavy reflux flowrate controller |
| $HRI$ | Heavy reflux interaction |
| $I$ | Interaction module |
| $IP_1$ | First isotherm parameter, *mol/(kg.kPa)* |
| $IP_2$ | Second isotherm parameter, *1/kPa* |
| $\overline{K}_{K,i}$ | Local Henry's coefficient obtained from equilibrium isotherms, *dimensionless* |
| $k_{MTC}$ | Lumped, effective mass transfer coefficient, *1/s* |
| $k_f$ | Film resistance coefficient , *1/s* |
| $L_{bed}$ | Length of each adsorption column, $m$ |
| $LP$ | Light product |
| $LPFC$ | Light product flowrate controller |
| $LR$ | Light reflux |
| $LRI$ | Light reflux interaction |
| $L_{RS}$ | Length of rectifying section of the column, $m$ |
| $L_{SS}$ | Length of stripping section of the column, $m$ |
| $M_{ads}$ | Adsorbent weight, *kg* |
| $M_W$ | Molecular weight, *kg/kmol* |
| $N$ | Number of moles, *kmol* |
| $N_{BD}$ | Total number of moles of gas released during Blowdown step, *kmol* |
| $N_{PR}$ | Total number of moles of gas fed to the column during Pressurization step, *kmol* |

https://doi.org/10.1016/j.ces.2014.09.013

| | |
|---|---|
| $P$ | Pressure, total pressure, final pressure, *kPa* |
| $p$ | Partial pressure, *kPa* |
| $P_{BD,end}$ | Pressure at the end of blowdown step, *kPa* |
| $PDE$ | Partial differential equation |
| $P_H$ | High pressure, *kPa* |
| $PI$ | Pressure interaction |
| PID | Proportional-Integral-Derivative |
| $P_L$ | Low pressure, *kPa* |
| $PR$ | Pressurization step |
| PSA | Pressure swing adsorption |
| $PU$ | Purge step |
| $Q$ | Flowrate, *sccm* |
| $Q_{BD}$ | Flowrate of gas released during blowdown step, *sccm* |
| $Q_{BD/PR}$ | Flowrate of gas released during blowdown step or flowrate of gas fed to the column during pressurization step, *sccm* |
| $Q_F$ | Flowrate of feed gas, *sccm* |
| $Q_{H,out}$ | Flowrate of gas released from the low pressure column during feed step, *sccm* |
| $Q_{HP}$ | Flowrate of heavy product, *sccm* |
| $Q_{HR}$ | Flowrate of heavy reflux, *sccm* |
| $\bar{q}_i$ | Particle-average concentration of species $i$ in adsorbed phase per unit mass of solid, *kmol/kg* |
| $q_i^*$ | Adsorbent loading of component $i$ which is in equilibrium with the gas-phase composition, *kmol/kg* |
| $Q_{L,out}$ | Flowrate of gas released from the column during purge step, *sccm* |
| $Q_{LP}$ | Flowrate of light product, *sccm* |
| $Q_{LR}$ | Flowrate of light reflux, *sccm* |
| $Q_{PR}$ | Flowrate of gas fed to the column during pressurization step, *sccm* |
| $R$ | Universal gas constant, *(kPa.m$^3$)/(kmol.K)* |
| $\mathbb{R}$ | represents that the interaction module is recording information |
| $Re$ | Reynolds number, *dimensionless* |
| $r_P$ | Radius of adsorbent particle, *mm* |
| $r_{P,mac}$ | Radius of macropores in adsorbent particle, *m* |
| $RS$ | Rectifying section |
| *s* | represents time in seconds |
| *sec* | represents time in seconds |
| *sccm* | represents flowrate in standard cubic centimeters per minute, *std cm$^3$/min* |
| $Sh$ | Sherwood number, *dimensionless* |
| $Sc$ | Schmid number, *dimensionless* |
| $SS$ | Stripping section |
| $T$ | Temperature, *K* |
| $t$ | Time, *s* |
| $t_{cycle}$ | Time of one DR-PS-A cycle, *s* |
| $t_{FE}$ | Feed step duration, *s* |
| $t_{FE/PU}$ | Feed or purge step duration, *s* |
| $t_{PU}$ | Purge step duration, *s* |
| $V_{bed}$ | Adsorbent bed volume, *m$^3$* |

https://doi.org/10.1016/j.ces.2014.09.013

| | |
|---|---|
| $V_F$ | represents the valve through which feed material flows |
| $v_g$ | Gas-phase superficial velocity, *m/s* |
| $V_{meso+macro}$ | Mesoporous and macroporous volumes, *$m^3$/kg* |
| $y$ | Mole fraction of heavy component in any stream, final composition (in terms of mole fraction of heavy component), specific concentration value, *dimensionless* |
| $y_{C_2H_6}$ | Mole fraction of $C_2H_6$, *dimensionless* |
| $\bar{y}$ | Average mole fraction of heavy component in any stream, *dimensionless* |
| $y_i$ | Bulk gas-phase mole fraction of component $i$, *dimensionless* |
| $y_F$ | Mole fraction of heavy component in binary feed gas mixture, *dimensionless* |
| $\bar{y}_{HP}$ | Average mole fraction of heavy component in heavy product stream, *dimensionless* |
| $y_{HP}$ | Mole fraction of heavy component in heavy product stream, *dimensionless* |
| $\bar{y}_{LP}$ | Average mole fraction of heavy component in light product stream, *dimensionless* |
| $(1-\bar{y}_{LP})$ | Average mole fraction of light component in light product stream, *dimensionless* |
| $Z$ | axial co-ordinate normalized with respect to column length, *dimensionless* |
| $z$ | position along the length of the adsorption column, axial co-ordinate, *m* |
| $Z=0$ | Stripping section end of the column, light material is either injected-in or is released at this position during the process, *dimensionless* |
| $Z=1$ | Rectifying section end of the column, heavy material is either injected-in or is released at this position during the process, *dimensionless* |
| $Z_F$ | Feed injection position along the length of the adsorption column, *dimensionless* |

## *Greek letters*

| | |
|---|---|
| $\varepsilon_i$ | Interstitial (or external) porosity of the adsorbent, *dimensionless* |
| $\varepsilon_P$ | Adsorbent particle porosity, *dimensionless* |
| $\varepsilon_T$ | Total bed voidage, *dimensionless* |
| $\psi$ | Shape factor of adsorbent particle, *dimensionless* |
| $\rho$ | Density, *$kg/m^3$* |
| $\rho_B$ | Bulk density of adsorbent, *$kg/m^3$* |
| $\rho_g$ | Molar gas-phase density, *$kmol/m^3$* |
| $\rho_S$ | Solid density of adsorbent, *$kg/m^3$* |
| $\tau$ | Tortuosity of adsorbent particle, *dimensionless* |
| $\mu$ | Dynamic viscosity, *kg/(m.s)* |

## *Symbols*

| | |
|---|---|
| × | represents closed valve or nonfunctional interaction |
| ✓ | represents open valve at designated or controlled flowrate |

https://doi.org/10.1016/j.ces.2014.09.013

## References


Bhatt, T.S., Storti, G., Rota, R., 2013. Optimal design of dual-reflux pressure swing adsorption units via equilibrium theory. Chemical Engineering Science 102, 42-55.

Diagne, D., Goto, M., Hirosi, T., 1994. New PSA process with intermediate feed inlet position and operated with dual refluxes: application to carbon dioxide removal and enrichment. Journal of Chemical Engineering Japan 27 (1), 85–89.

Diagne, D., Goto, M., Hirosi, T., 1995a. Experimental study of simultaneous removal and concentration of CO2 by an improved pressure swing adsorption process. Energy Conversion and Management 36, 431–434.

Diagne, D., Goto, M., Hirosi, T., 1995b. Parametric studies on CO2 separation and recovery by a dual reflux PSA process consisting of both rectifying and stripping sections. Industrial and Engineering Chemistry Research 34, 3083–3089.

Diagne, D., Goto, M., Hirosi, T., 1996. Numerical analysis of a dual refluxed PSA process during simultaneous removal and concentration of carbon dioxide dilute gas from air. Journal of Chemical Technology and Biotechnology 65, 29–38.

Ebner, A.D., Ritter, J.A., 2002. Equilibrium theory analysis of rectifying PSA for heavy component production. A.I.Ch.E. Journal 48 (8), 1679–1691.

Ebner, A.D., Ritter, J.A., 2004. Equilibrium theory analysis of dual reflux PSA for separation of a binary mixture. A.I.Ch.E. Journal 50 (10), 2418–2429.

Ergun, S. (1952). Fluid flow through packed columns. Chemical Engineering Progress, 48(2), 89-94.

Hou, X., Liu, X., Liu, Z., Yan, F., Yuan, X.J., 2010. Flow field simulation and experimental evaluation of carbon canister based on FLUENT. Computational Intelligence and Software Engineering (CiSE), International Conference 1, 4.

Kearns, D.T., Webley, P.A., 2006. Modeling and evaluation of dual-reflux pressure swing adsorption cycles: Part I. Mathematical models. Chemical Engineering Science 61, 7223-33.

Knaebel, K.S., Hill, F.B., 1985. Pressure swing adsorption: development of an equilibrium theory for gas separations. Chemical Engineering Science 40 (12), 2351–2360.

Leavitt, F.W., 1992. Duplex Adsorption Process. US Patent 5,085,674.

McIntyre, J.A., Holland, C.E., Ritter, J.A., 2002. High enrichment and recovery of dilute hydrocarbons by dual-reflux pressure-swing adsorption. Industrial and Engineering Chemistry Research 41, 3499–3504.

McIntyre, J.A., Ebner, A.D., Ritter, J.A., 2010. Experimental study of a dual reflux enriching pressure swing adsorption process for concentrating dilute feed streams. Industrial & Engineering Chemistry Research 49 (4), 1848–1858.

Rhee, H.K., Aris R., and Amundson N.R., 1986. First-order partial differential equations, Vol. 1, Prentice-Hall, Englewood Cliffs, NJ.

Ruthven, D.M., Farooq, S., Knaebel, K.S., 1994. Pressure Swing Adsorption, VCH Publishers, New York, NY.

Sivakumar, S.V., Rao, D.P., 2011a. Modified Duplex PSA. 1. Sharp separation and process intensification for $CO_2$–$N_2$–13X zeolite system. Industrial & Engineering Chemistry Research 50, 3426–3436.


https://doi.org/10.1016/j.ces.2014.09.013

Sivakumar, S.V., Rao, D.P., 2011b. Modified duplex PSA. 2. Sharp separation and process intensification for $N_2$–$O_2$–5A zeolite system. Industrial & Engineering Chemistry Research 50, 3437–3445.

Sivakumar, S.V., Rao, D.P., 2012. Adsorptive separation of gas mixtures: mechanistic view, sharp separation and process intensification. Chemical Engineering and Processing 53, 31–52.

Skarstrom, C.W., 1959. Use of adsorption phenomena in automatic plant-type gas analysers. Annals of the New York Academy of Sciences 72, 751–763.

Spoorthi, G., Thakur, R.S., Kaistha, N., Rao, D.P., 2011. Process intensification in PSA processes for upgrading synthetic landfill and lean natural gases. Adsorption 17, 121–133.

Subramanian, D., Ritter, J.A., 1997. Equilibrium theory for solvent vapor recovery by pressure swing adsorption: analytical solution for process performance. Chemical Engineering Science 52 (18), 3147–3160.

Thakur, R.S., Kaistha, N., Rao, D.P., 2011. Process intensification in duplex pressure swing adsorption. Computers and Chemical Engineering 35, 973–983.

Tolles, E.D., Collins, E.A., Williams, R.S., 2009. Packed adsorbent systems with low flow resistance. International patent PCT/US2009/041002.

Wilhelm, M., Soltmann, C., Koch, D., Grathwohl, G., 2005. Ceramers—functional materials for adsorption techniques. Journal of the European Ceramic Society, 25 (2), 271-276.

Yang, R. T., Doong, S. J., 1985. Gas separation by pressure swing adsorption: A pore-diffusion model for bulk separation. AIChE 31 (11), 1829–1842.

Yoshida, M., Ritter, J.A., Kodama, A., Goto, M., Hirose, T., 2003. Enriching reflux and parallel equalization PSA process for concentrating trace components in air. Industrial and Engineering Chemistry Research 42, 1795–1803.

Zhang, W., Thompson, K. E., Reed, A. H., Beenken, L., 2006. Relationship between packing structure and porosity in fixed beds of equilateral cylindrical particles. Chemical Engineering Science, 61(24), 8060-8074.

https://doi.org/10.1016/j.ces.2014.09.013

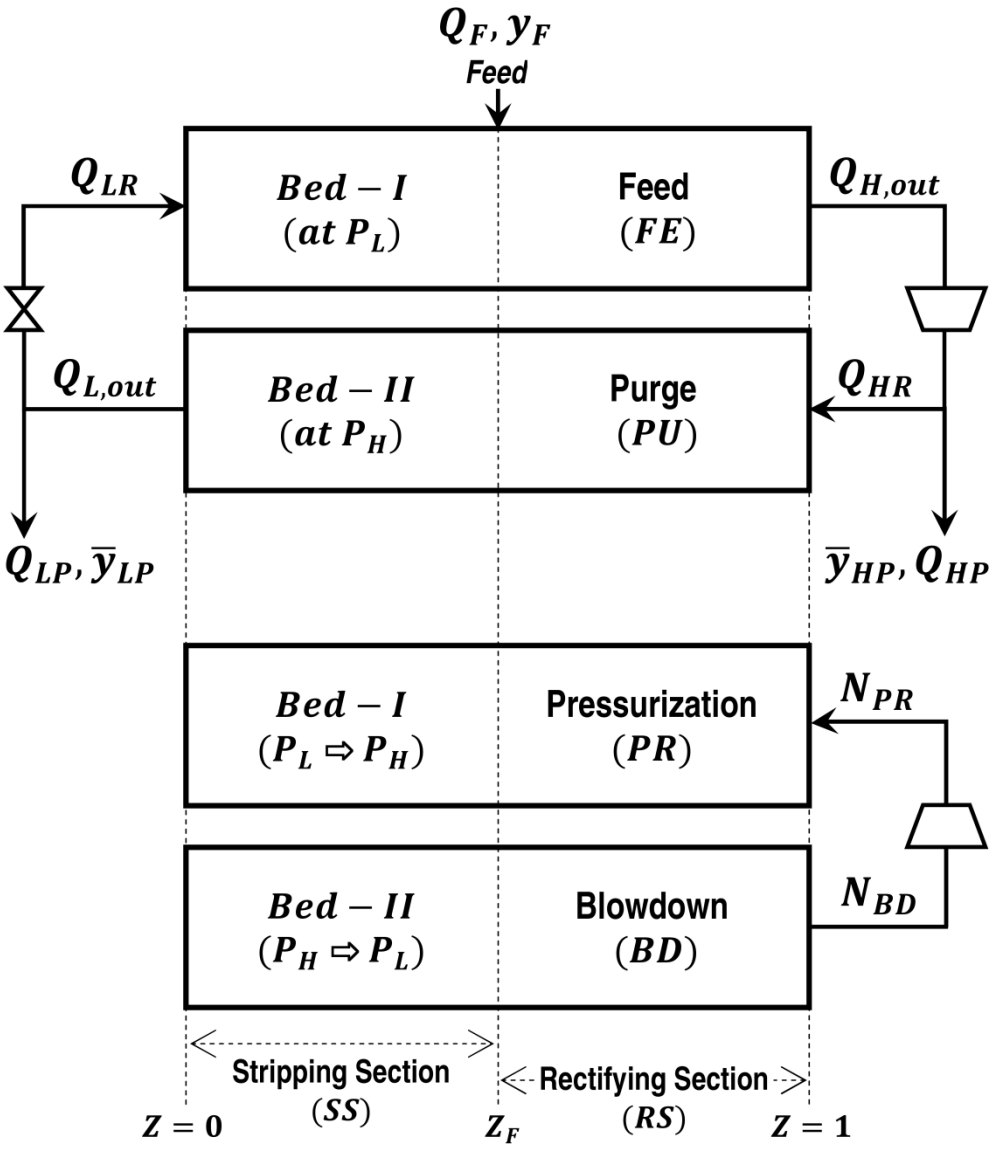


Fig. 1. DR-PL-A cycle steps and flows.

https://doi.org/10.1016/j.ces.2014.09.013

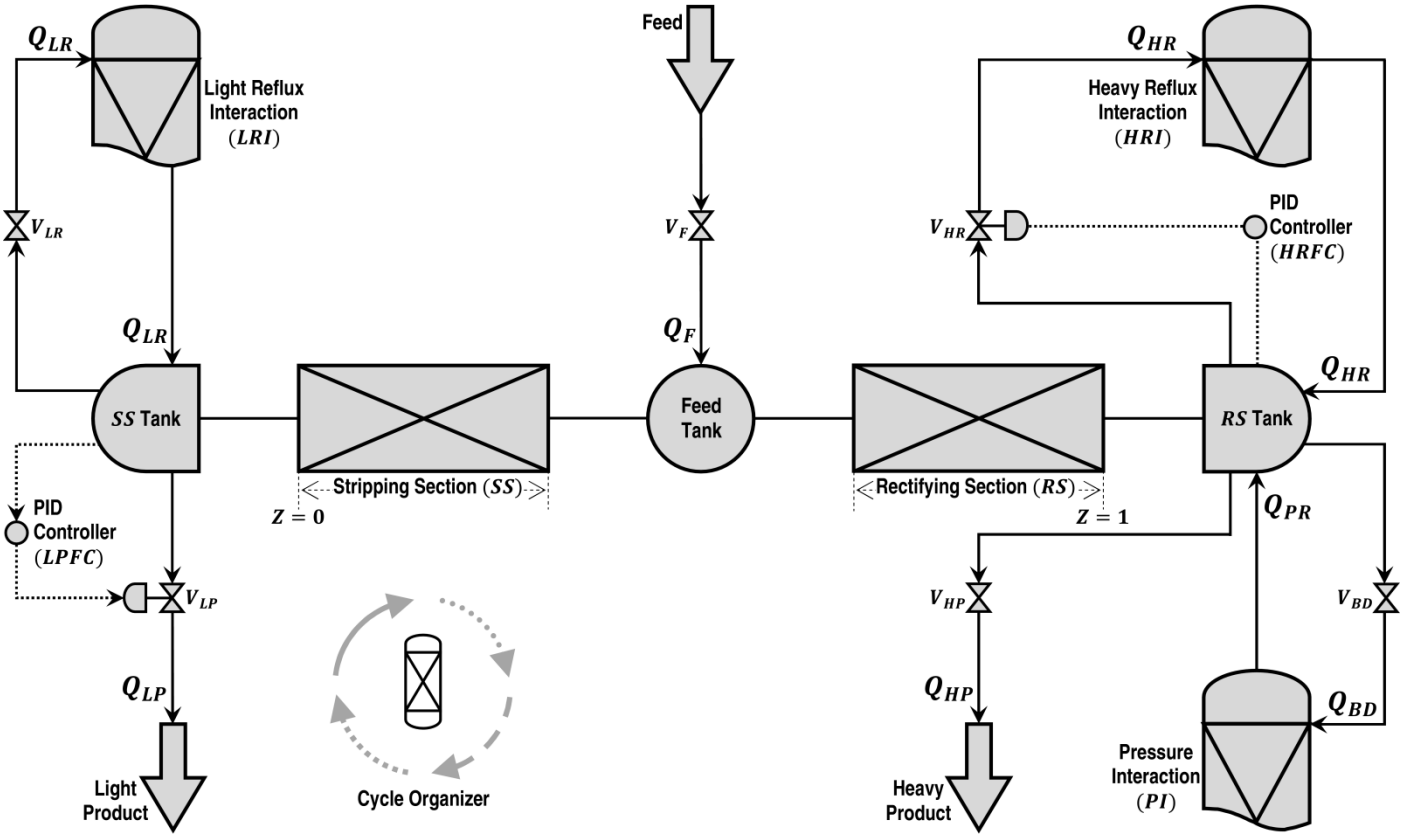


Fig. 2. Schematic representation of DR-PL-A process simulation flowsheet.

https://doi.org/10.1016/j.ces.2014.09.013

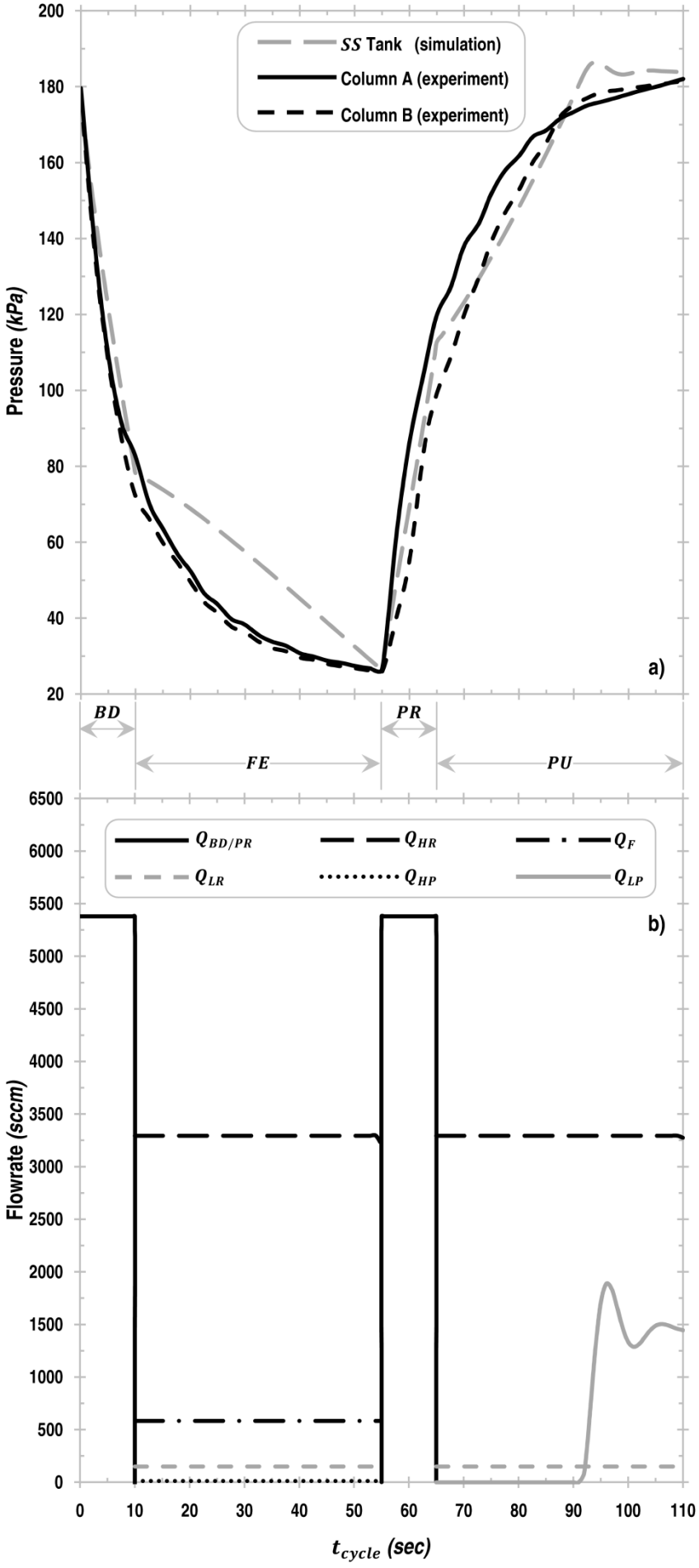


Fig. 3. Base case (Run # 1) results at $\boldsymbol{CSS}$ during one DR-PL-A cycle. a) Simulation and experimental pressure profiles and b) simulated flow pattern of various streams ($\boldsymbol{FE}$: Feed; $\boldsymbol{BD}$: Blowdown; $\boldsymbol{PR}$: Pressurization and; $\boldsymbol{PU}$: Purge step).

https://doi.org/10.1016/j.ces.2014.09.013

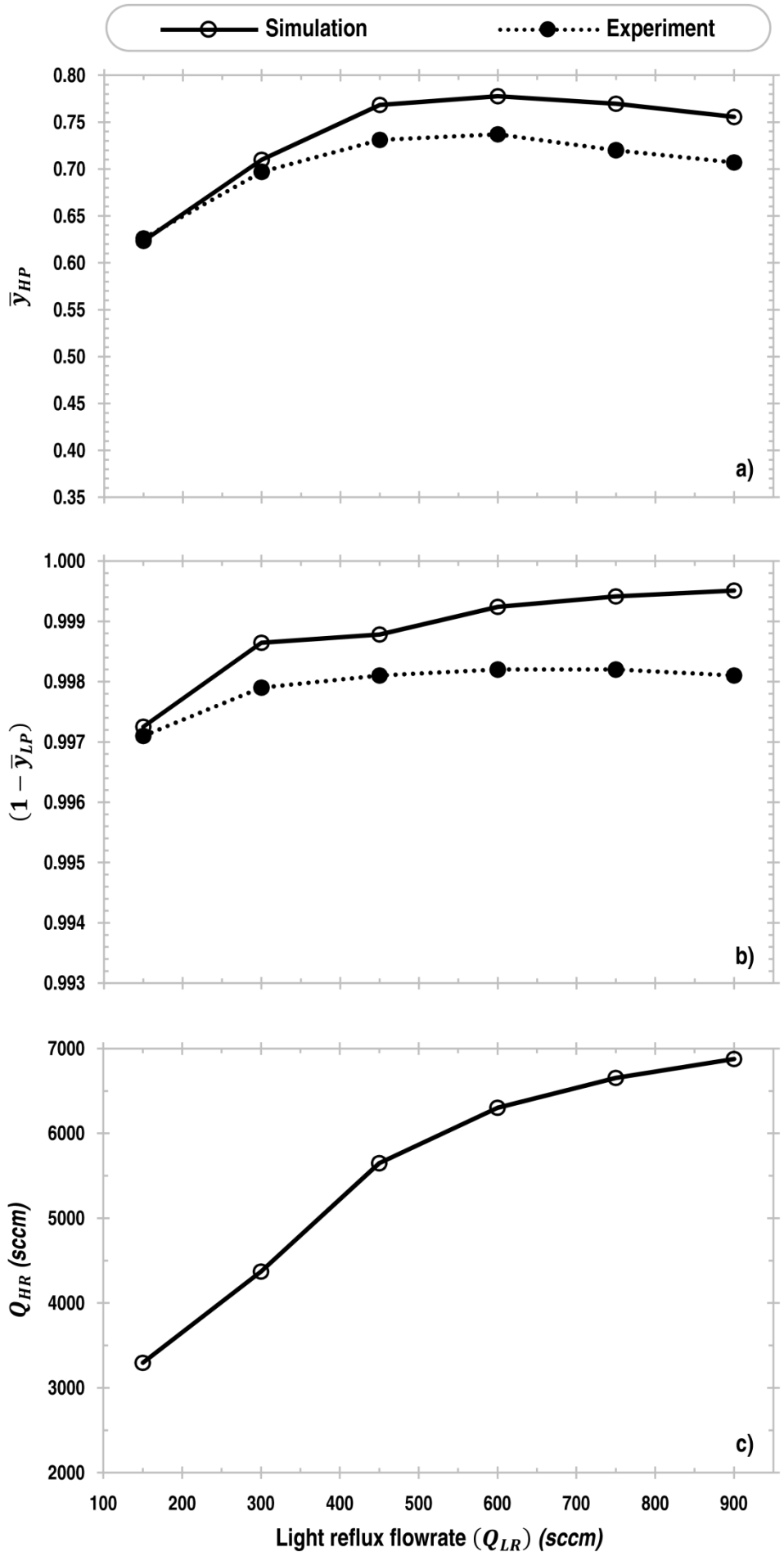


Fig. 4. Simulation and/or experimental (McIntyre et al., 2010) results at $\boldsymbol{CSS}$ for Run # 1 to 6 showing the effect of light reflux flowrate ($\boldsymbol{Q_{LR}}$) on: a) average $\boldsymbol{C_2H_6}$ mole fraction in heavy product ($\bar{y}_{HP}$); b) average mole fraction of $\boldsymbol{N_2}$ in light product ($\boldsymbol{1-\bar{y}_{LP}}$) and; c) heavy reflux flowrates ($\boldsymbol{Q_{HR}}$).

https://doi.org/10.1016/j.ces.2014.09.013

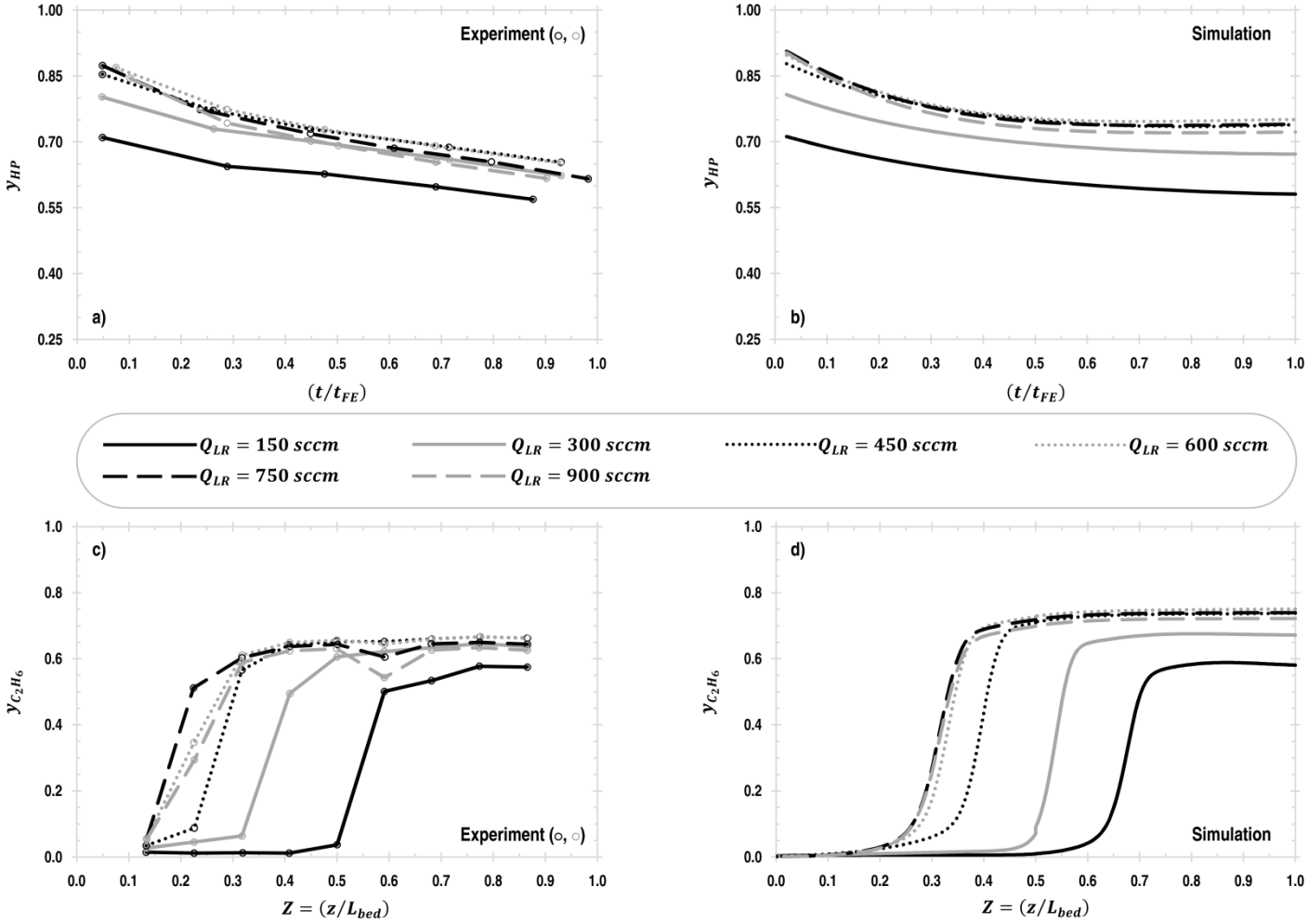


Fig. 5. Results at cyclic steady state ($\boldsymbol{CSS}$) for Run # 1 to 6 showing the effect of light reflux flowrate ($\boldsymbol{Q_{LR}}$) on: a) ethane mole fraction profile in heavy product ($\boldsymbol{y_{HP}}$) measured by the experimenters (McIntyre et al., 2010) during feed step ($\boldsymbol{FE}$); b) model predicted ethane mole fraction profile in heavy product ($\boldsymbol{y_{HP}}$) during feed step ($\boldsymbol{FE}$); c) ethane mole fraction profile in the column $\left(\boldsymbol{y_{C_2H_6}}\right)$ at the *end* of high pressure purge step ($\boldsymbol{PU}$) measured by the experimenters (McIntyre et al., 2010) and; d) model predicted ethane mole fraction profile in the column $\left(\boldsymbol{y_{C_2H_6}}\right)$ at the *end* of high pressure purge step ($\boldsymbol{PU}$).

https://doi.org/10.1016/j.ces.2014.09.013

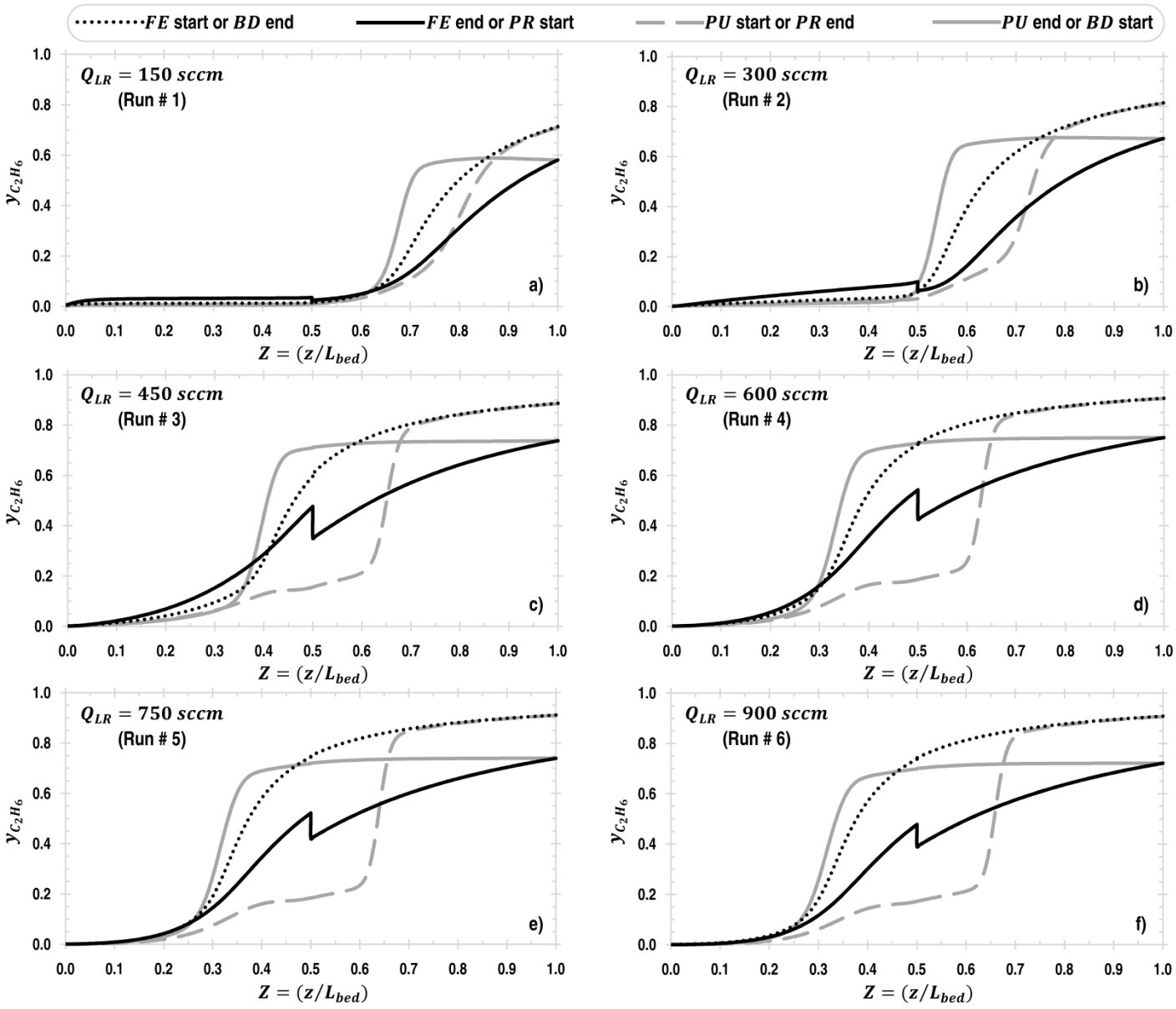


Fig. 6. Model predicted cyclic steady state ($\boldsymbol{CSS}$) column composition profiles at the *beginning* (start) and *end* of each DR-PL-A cycle step for Run # 1 to 6 ($\boldsymbol{FE}$: Feed; $\boldsymbol{BD}$: Blowdown; $\boldsymbol{PR}$: Pressurization and; $\boldsymbol{PU}$: Purge step).

https://doi.org/10.1016/j.ces.2014.09.013

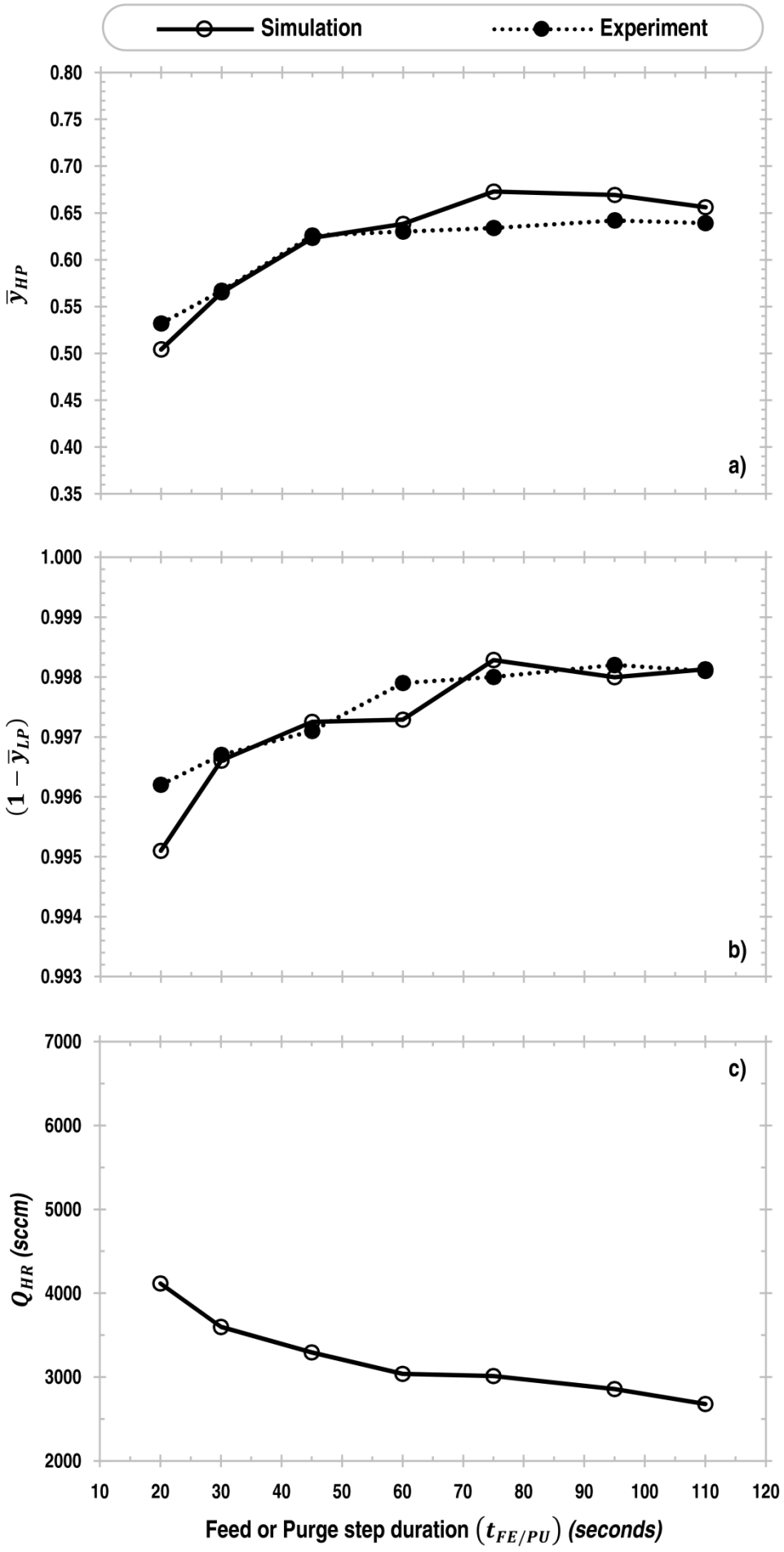


738

739 Fig. 7. Simulation and/or experimental (McIntyre et al., 2010) results at $\boldsymbol{CSS}$ for Run # 7, 8, 1 and 9 to 12; showing the effect of feed or
740 purge step duration $(\boldsymbol{t_{FE/PU}})$ on: a) average $\boldsymbol{C_2H_6}$ mole fraction in heavy product $(\bar{\boldsymbol{y}}_{\boldsymbol{HP}})$; b) average mole fraction of $\boldsymbol{N_2}$ in light
741 product $(\boldsymbol{1-\bar{y}_{LP}})$ and; c) heavy reflux flowrates $(\boldsymbol{Q_{HR}})$.

https://doi.org/10.1016/j.ces.2014.09.013

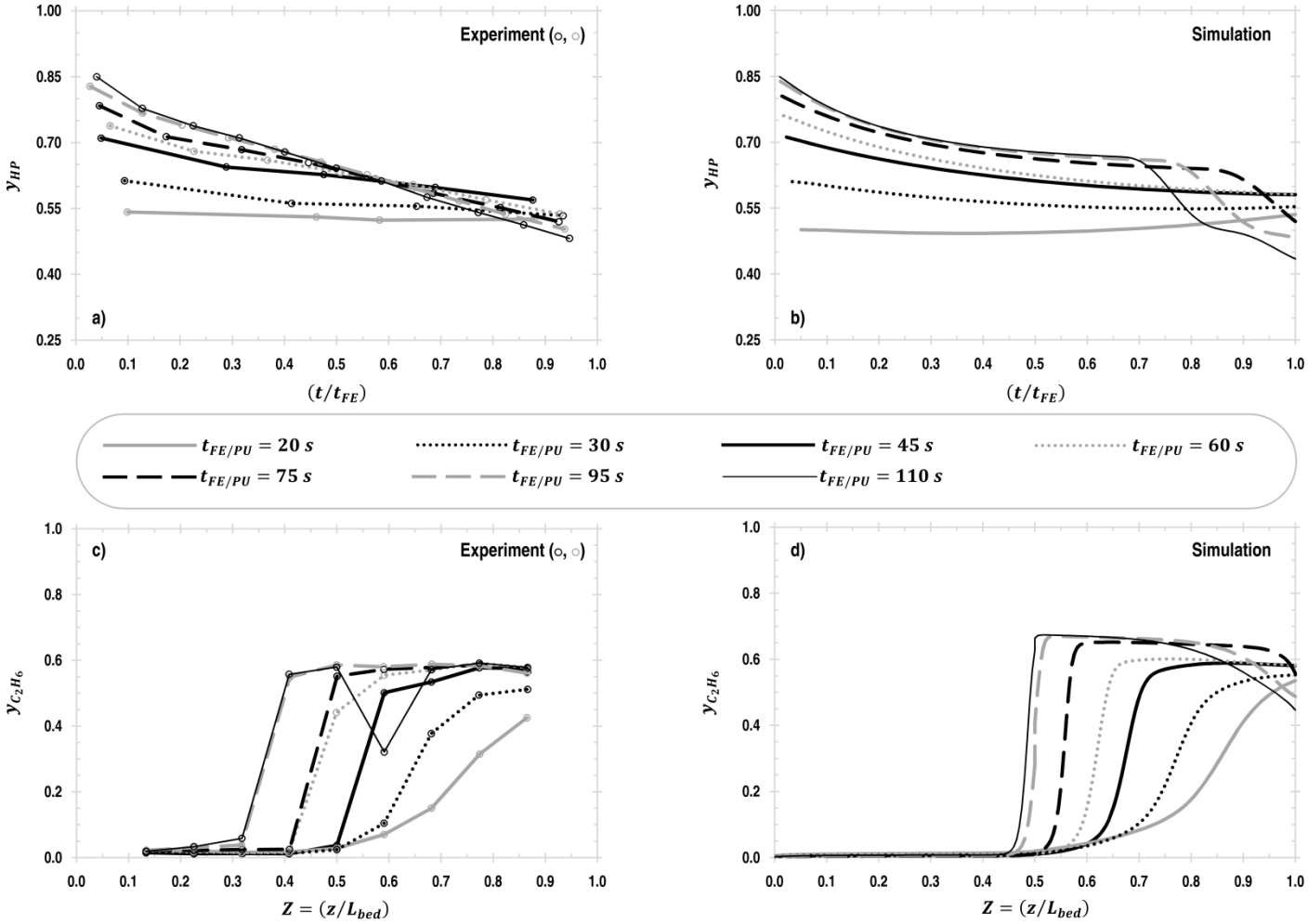


Fig. 8. Results at cyclic steady state ($\boldsymbol{CSS}$) for Run # 7, 8, 1 and 9 to 12; showing the effect of feed or purge step duration $\left(\boldsymbol{t_{FE/PU}}\right)$ on: a) ethane mole fraction profile in heavy product ($\boldsymbol{y_{HP}}$) measured by the experimenters (McIntyre et al., 2010) during feed step ($\boldsymbol{FE}$); b) model predicted ethane mole fraction profile in heavy product ($\boldsymbol{y_{HP}}$) during feed step ($\boldsymbol{FE}$); c) ethane mole fraction profile in the column $\left(\boldsymbol{y_{C_2H_6}}\right)$ at the *end* of high pressure purge step ($\boldsymbol{PU}$) measured by the experimenters (McIntyre et al., 2010) and; d) model predicted ethane mole fraction profile in the column $\left(\boldsymbol{y_{C_2H_6}}\right)$ at the *end* of high pressure purge step ($\boldsymbol{PU}$).

https://doi.org/10.1016/j.ces.2014.09.013

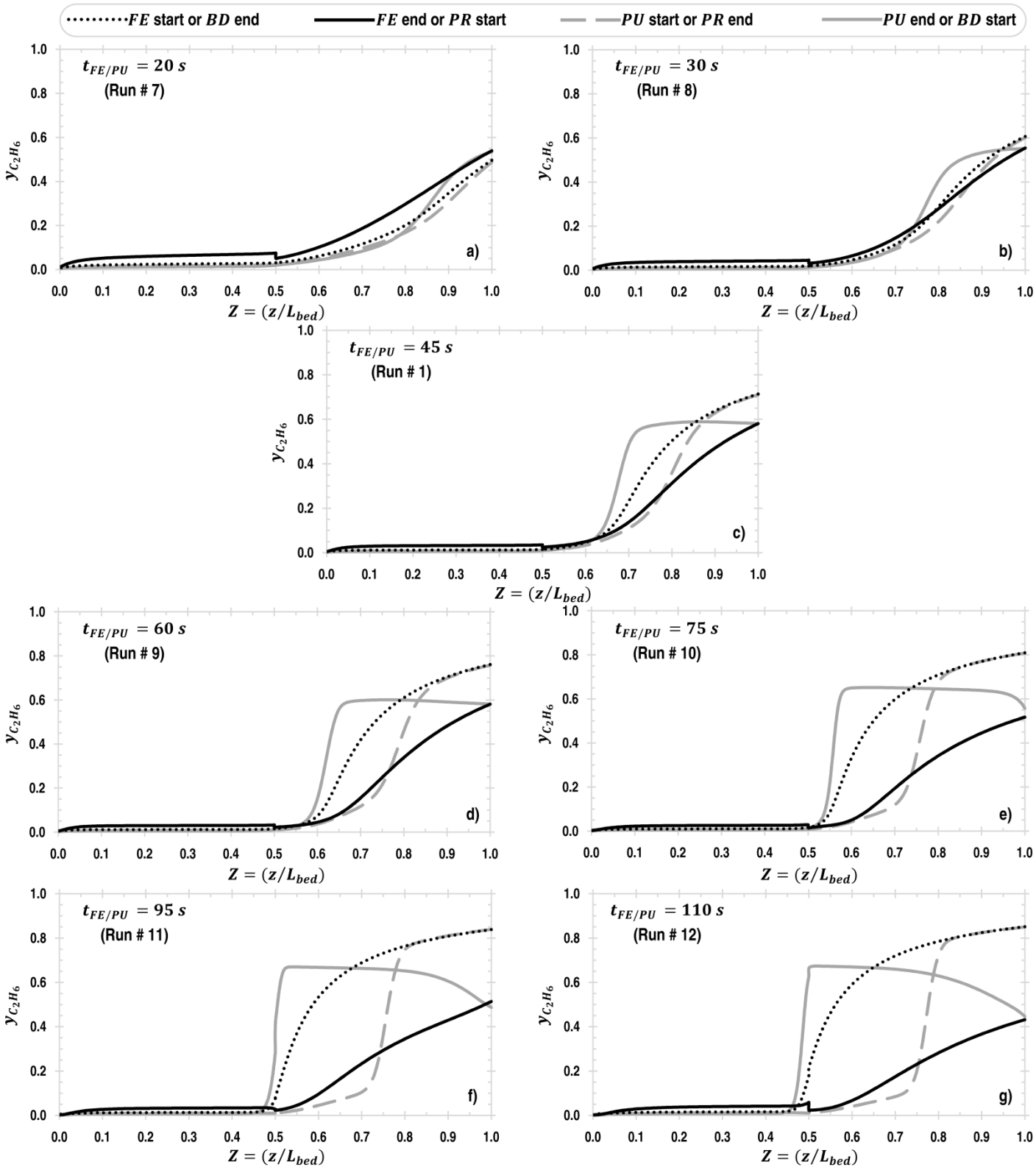


Fig. 9. Model predicted cyclic steady state ($\boldsymbol{CSS}$) column composition profiles at the *beginning* (start) and *end* of each DR-PL-A cycle step for Run # 7, 8, 1 and 9 to 12 ($\boldsymbol{FE}$: Feed; $\boldsymbol{BD}$: Blowdown; $\boldsymbol{PR}$: Pressurization and; $\boldsymbol{PU}$: Purge step).

https://doi.org/10.1016/j.ces.2014.09.013

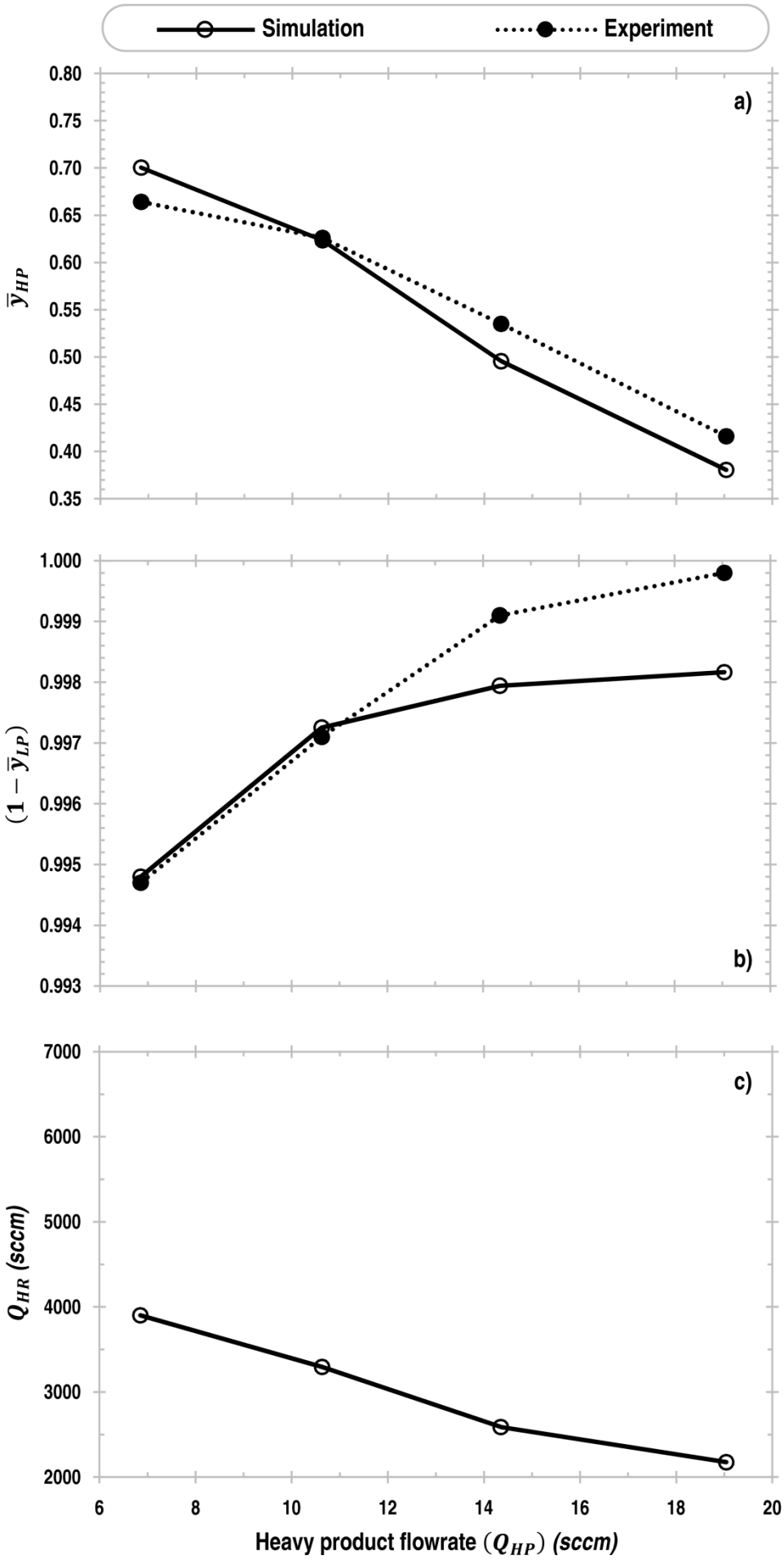


Fig. 10. Simulation and/or experimental (McIntyre et al., 2010) results at $\boldsymbol{CSS}$ for Run # 13, 1, 14 and 15 showing the effect of heavy product flowrate $(\boldsymbol{Q_{HP}})$ on: a) average $\boldsymbol{C_2H_6}$ mole fraction in heavy product $(\bar{\boldsymbol{y}}_{\boldsymbol{HP}})$; b) average mole fraction of $\boldsymbol{N_2}$ in light product $(\boldsymbol{1-\bar{y}_{LP}})$ and; c) heavy reflux flowrates $(\boldsymbol{Q_{HR}})$.

https://doi.org/10.1016/j.ces.2014.09.013

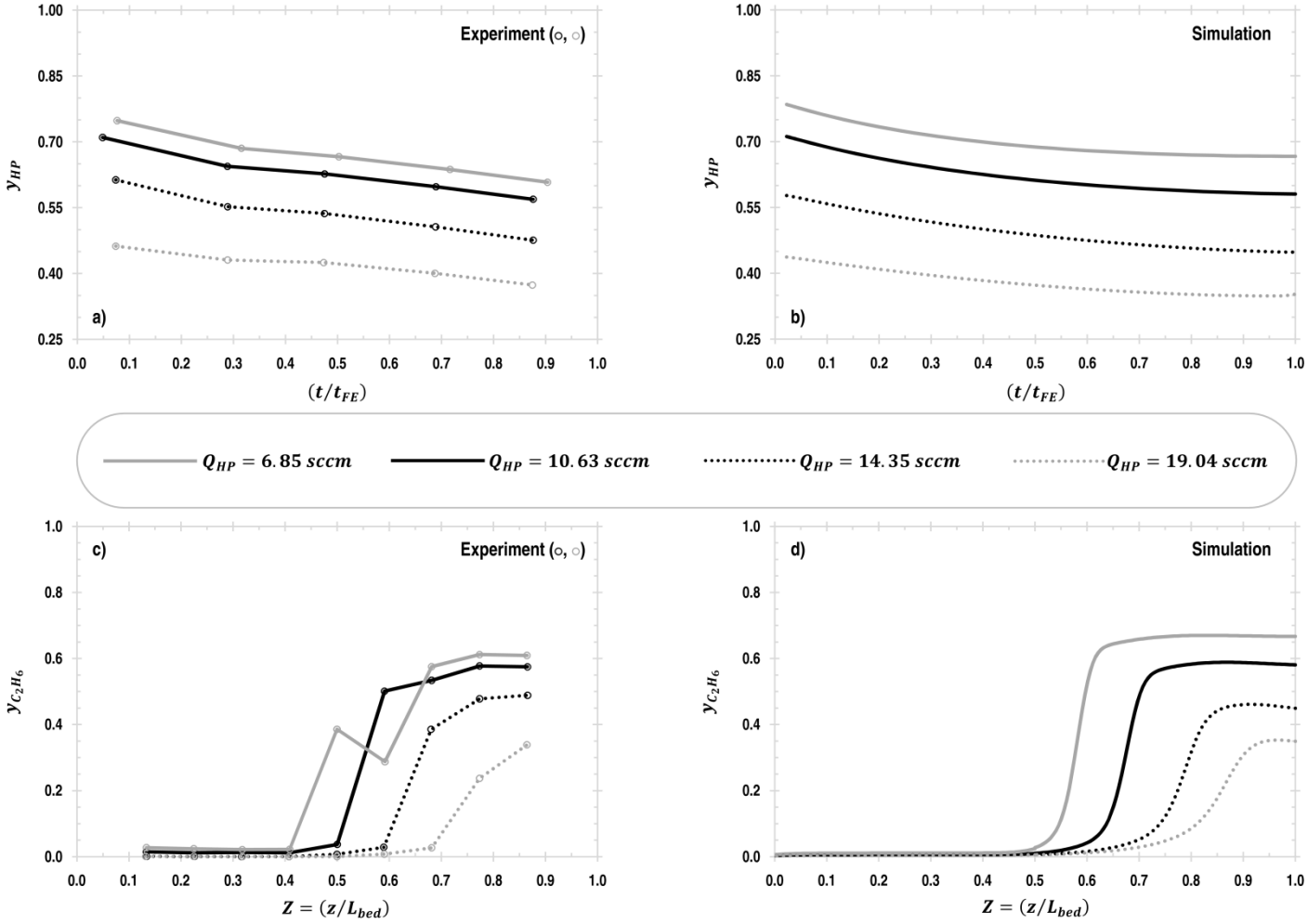


Fig. 11. Results at cyclic steady state ($\boldsymbol{CSS}$) for Run # 13, 1, 14 and 15 showing the effect of heavy product flowrate ($\boldsymbol{Q_{HP}}$) on: a) ethane mole fraction profile in heavy product ($\boldsymbol{y_{HP}}$) measured by the experimenters (McIntyre et al., 2010) during feed step ($\boldsymbol{FE}$); b) model predicted ethane mole fraction profile in heavy product ($\boldsymbol{y_{HP}}$) during feed step ($\boldsymbol{FE}$); c) ethane mole fraction profile in the column $\left(\boldsymbol{y_{C_2H_6}}\right)$ at the *end* of high pressure purge step ($\boldsymbol{PU}$) measured by the experimenters (McIntyre et al., 2010) and; d) model predicted ethane mole fraction profile in the column $\left(\boldsymbol{y_{C_2H_6}}\right)$ at the *end* of high pressure purge step ($\boldsymbol{PU}$).

https://doi.org/10.1016/j.ces.2014.09.013

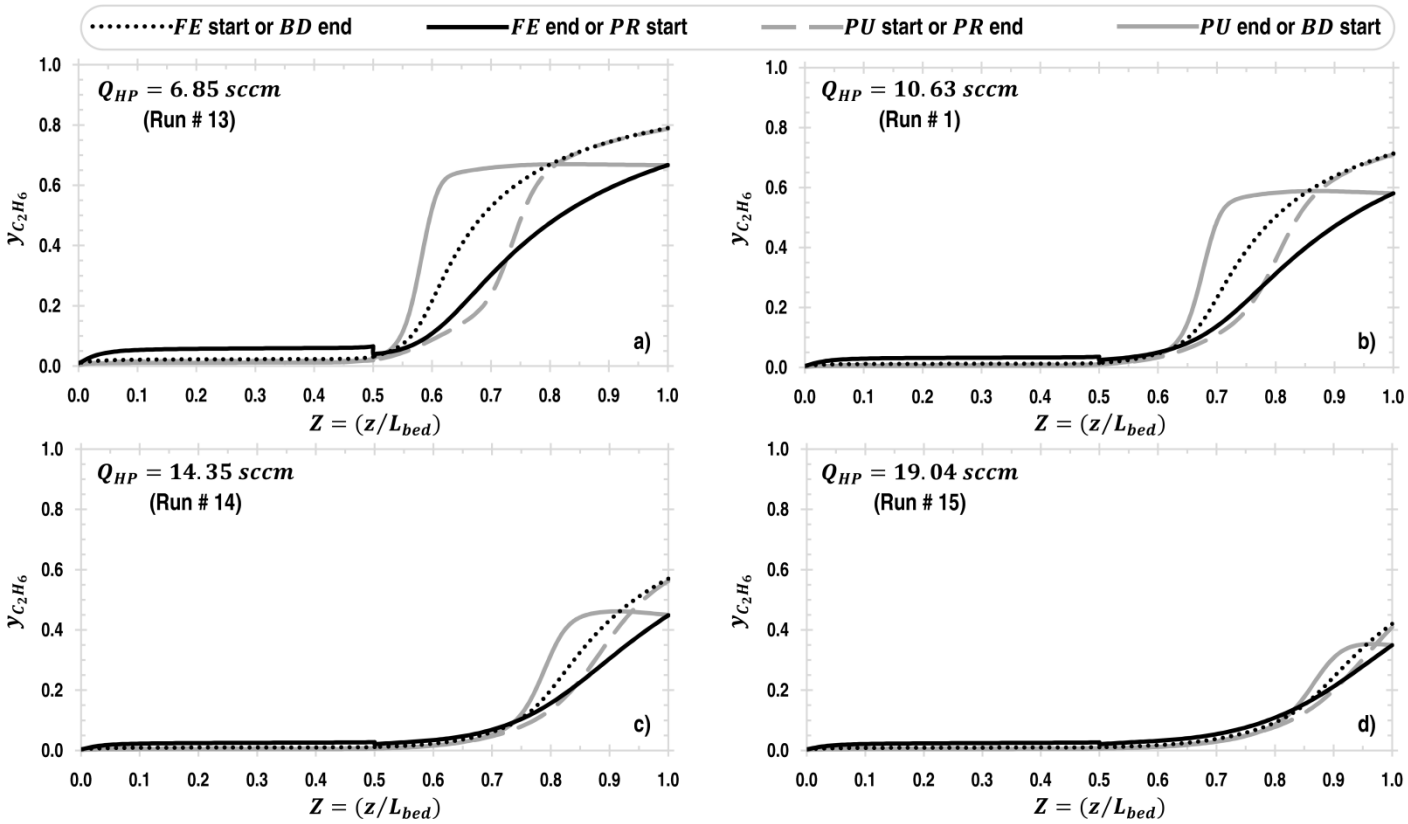


789

790

791 Fig. 12. Model predicted cyclic steady state (***CSS***) column composition profiles at the *beginning* (start) and *end* of each DR-PL-A
792 cycle step for Run # 13, 1, 14 and 15 (***FE***: Feed; ***BD***: Blowdown; ***PR***: Pressurization and; ***PU***: Purge step).

793

https://doi.org/10.1016/j.ces.2014.09.013

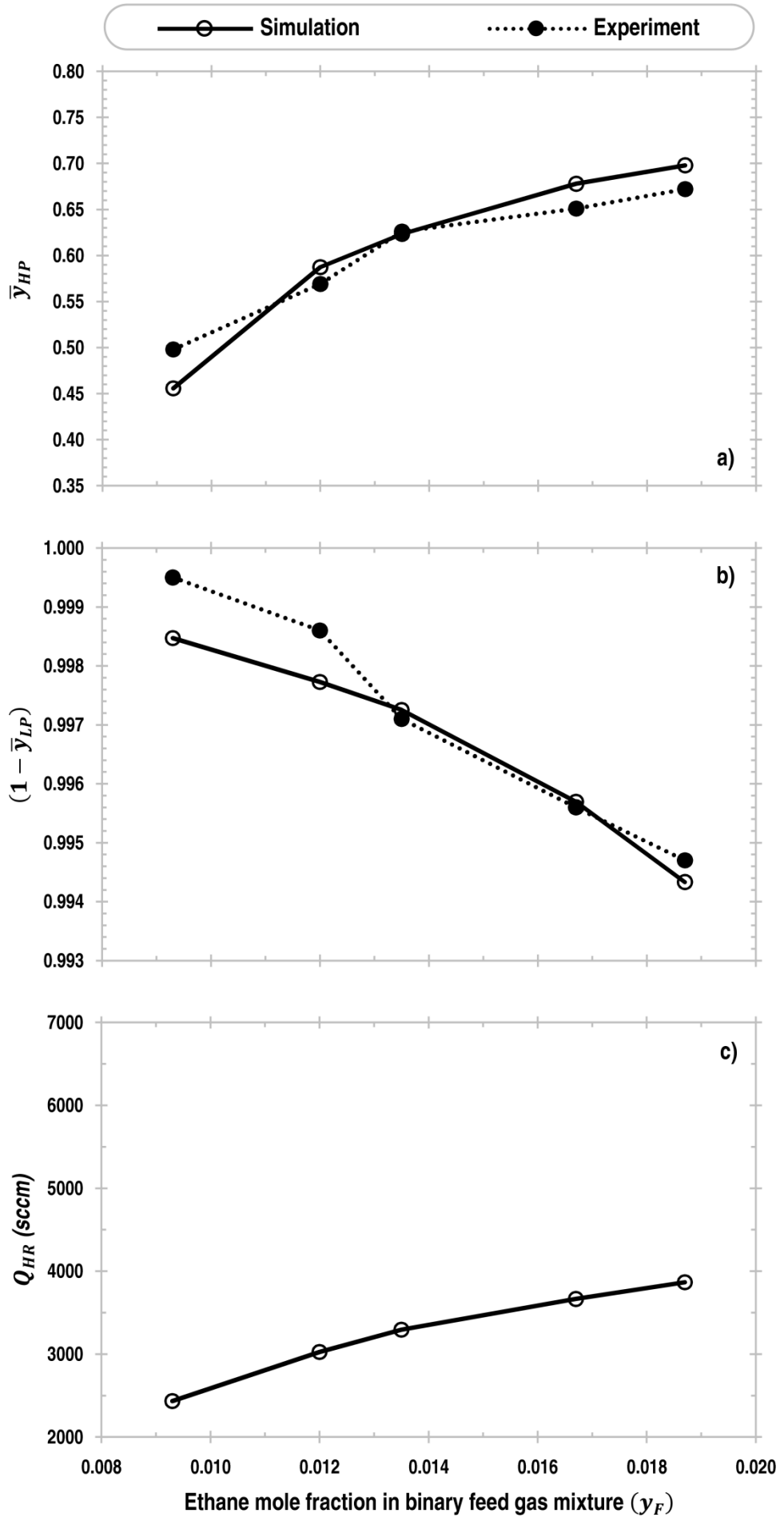


794

795 Fig. 13. Simulation and/or experimental (McIntyre et al., 2010) results at $\boldsymbol{CSS}$ for Run # 16, 17, 1, 18 and 19 showing the effect of
796 ethane mole fraction $(\boldsymbol{y_F})$ in binary feed gas mixture on: a) average $\boldsymbol{C_2H_6}$ mole fraction in heavy product $(\bar{\boldsymbol{y}}_{\boldsymbol{HP}})$; b) average mole
797 fraction of $\boldsymbol{N_2}$ in light product $(\boldsymbol{1-\bar{y}_{LP}})$ and; c) heavy reflux flowrates $(\boldsymbol{Q_{HR}})$.

https://doi.org/10.1016/j.ces.2014.09.013

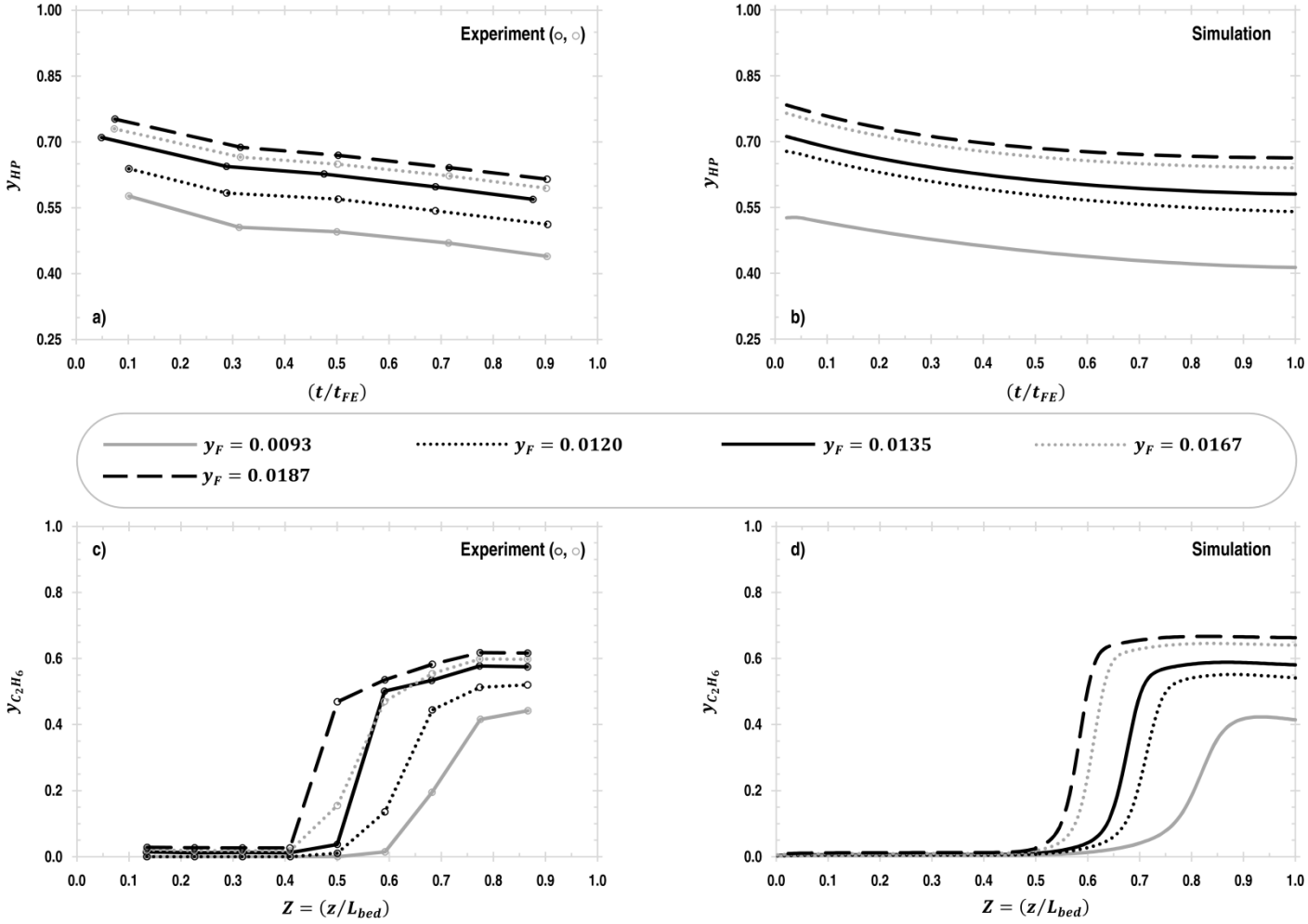


Fig. 14. Results at cyclic steady state ($\boldsymbol{CSS}$) for Run # 16, 17, 1, 18 and 19 showing the effect of ethane mole fraction ($\boldsymbol{y_F}$) in binary feed gas mixture on: a) ethane mole fraction profile in heavy product ($\boldsymbol{y_{HP}}$) measured by the experimenters (McIntyre et al., 2010) during feed step ($\boldsymbol{FE}$); b) model predicted ethane mole fraction profile in heavy product ($\boldsymbol{y_{HP}}$) during feed step ($\boldsymbol{FE}$); c) ethane mole fraction profile in the column $\left(\boldsymbol{y_{C_2H_6}}\right)$ at the *end* of high pressure purge step ($\boldsymbol{PU}$) measured by the experimenters (McIntyre et al., 2010) and; d) model predicted ethane mole fraction profile in the column $\left(\boldsymbol{y_{C_2H_6}}\right)$ at the *end* of high pressure purge step ($\boldsymbol{PU}$).

https://doi.org/10.1016/j.ces.2014.09.013

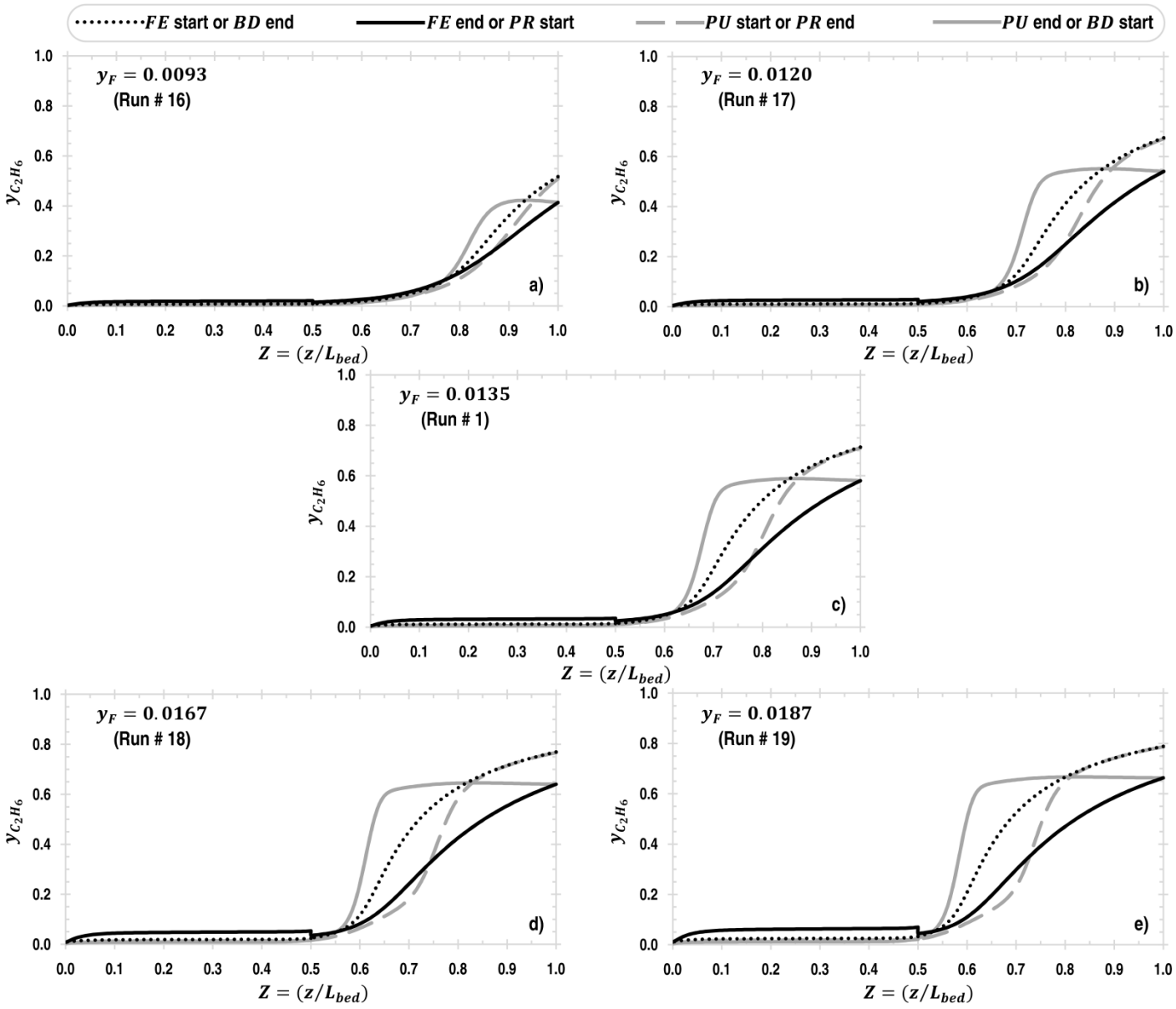


816

817

818 Fig. 15. Model predicted cyclic steady state ($\boldsymbol{CSS}$) column composition profiles at the *beginning* (start) and *end* of each DR-PL-A
819 cycle step for Run # 16, 17, 1, 18 and 19 ($\boldsymbol{FE}$: Feed; $\boldsymbol{BD}$: Blowdown; $\boldsymbol{PR}$: Pressurization and; $\boldsymbol{PU}$: Purge step).

https://doi.org/10.1016/j.ces.2014.09.013

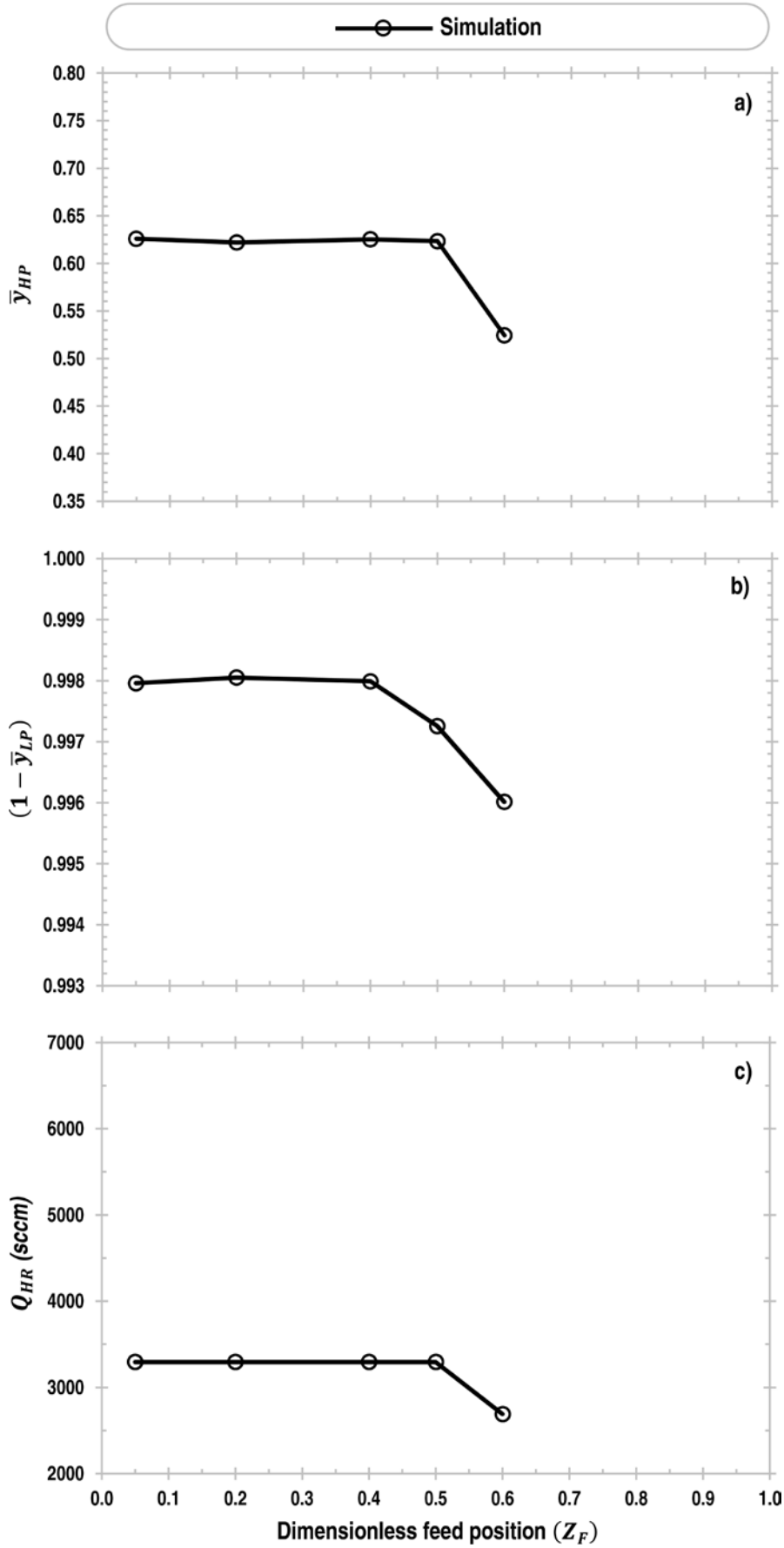


Fig. 16. Simulation results at $\boldsymbol{CSS}$ showing the effect of dimensionless feed position $(\boldsymbol{Z_F})$ on: a) average $\boldsymbol{C_2H_6}$ mole fraction in heavy product $(\bar{\boldsymbol{y}}_{\boldsymbol{HP}})$; b) average mole fraction of $\boldsymbol{N_2}$ in light product $(\boldsymbol{1-\bar{y}_{LP}})$ and; c) heavy reflux flowrates $(\boldsymbol{Q_{HR}})$.

https://doi.org/10.1016/j.ces.2014.09.013

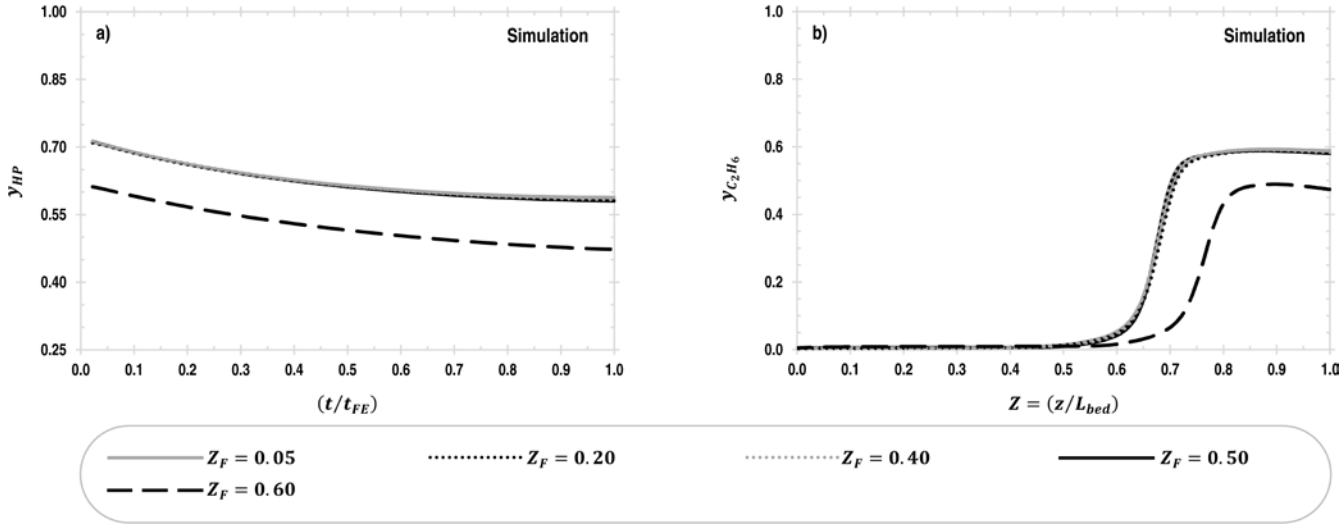


Fig. 17. Model predicted results at cyclic steady state ($\boldsymbol{CSS}$) showing the effect of dimensionless feed position ($\boldsymbol{Z_F}$) on: a) ethane mole fraction profile in heavy product ($\boldsymbol{y_{HP}}$) during feed step ($\boldsymbol{FE}$) and; b) ethane mole fraction profile in the column ($\boldsymbol{y_{C_2H_6}}$) at the *end* of high pressure purge step ($\boldsymbol{PU}$).

https://doi.org/10.1016/j.ces.2014.09.013

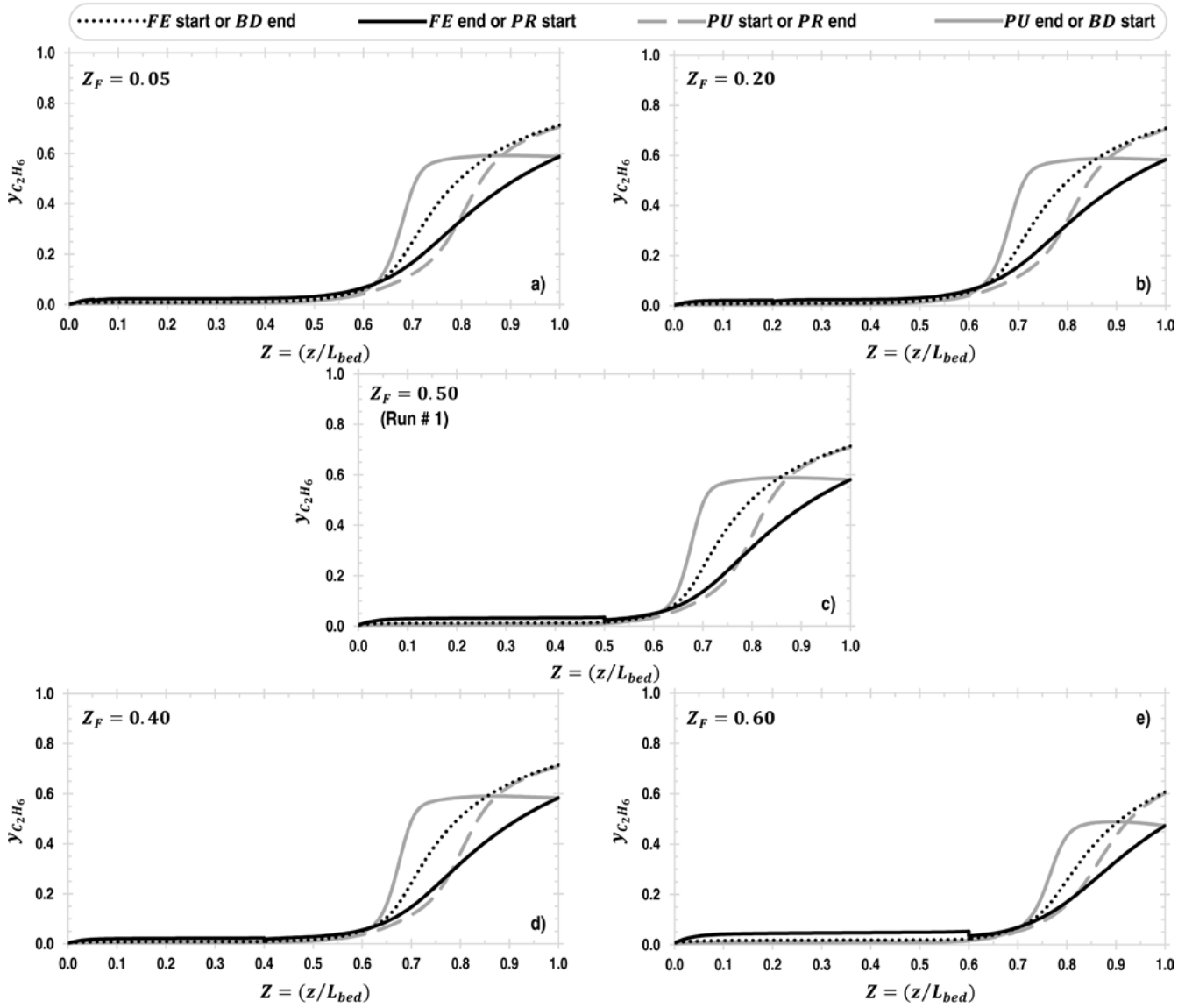


862
863
864 Fig. 18. Model predicted cyclic steady state (***CSS***) column composition profiles at the *beginning* (start) and *end* of each DR-PL-A
865 cycle step (***FE***: Feed; ***BD***: Blowdown; ***PR***: Pressurization and; ***PU***: Purge step).

866

https://doi.org/10.1016/j.ces.2014.09.013

| | | | |
|---|---|---|---|
| **Design parameters** | | | |
| Length of $SS$ | $L_{SS}$ | 0.435 | $m$ |
| Length of $RS$ | $L_{RS}$ | 0.435 | $m$ |
| Diameter of each column | $D_{column}$ | 0.024 | $m$ |
| Interstitial porosity | $\varepsilon_i$ | 0.32 | |
| **Operating parameters** | | | |
| Temperature | $T$ | 298.15 | $K$ |
| High pressure set point in $LPFC$ | $P_H$ | 184 | $kPa$ |
| Low pressure set point in $HRFC$ | $P_L$ | 26 | $kPa$ |
| Depressurization flowrate | $Q_{BD}$ | 5379.35 | $sccm$ |
| $BD$ end pressure | $P_{BD,end}$ | 78.75 | $kPa$ |
| **Adsorbent properties** | | | |
| Radius of adsorbent particle | $r_P$ | 1.31 | $mm$ |
| Particle porosity | $\varepsilon_P$ | 0.38 | |
| Bulk density | $\rho_B$ | 284.88 | $kg/m^3$ |
| Shape factor | $\psi$ | 1 | |
| Tortuosity | $\tau$ | 4 | |
| Macropore radius | $r_{P,mac}$ | 0.15 | $\mu m$ |
| **Isotherm data at 298.15 K** | | | |
| First isotherm parameter for $C_2H_6$ | $IP_{1,C_2H_6}$ | $9.14 \times 10^{-2}$ | $mol/(kg.kPa)$ |
| Second isotherm parameter for $C_2H_6$ | $IP_{2,C_2H_6}$ | $1.14 \times 10^{-2}$ | $1/kPa$ |
| First isotherm parameter for $N_2$ | $IP_{1,N_2}$ | $3.48 \times 10^{-3}$ | $mol/(kg.kPa)$ |
| Second isotherm parameter for $N_2$ | $IP_{2,N_2}$ | $1.25 \times 10^{-3}$ | $1/kPa$ |

Table 1. Parameter values used for all simulations.

https://doi.org/10.1016/j.ces.2014.09.013

| Run # | $y_F$ | $Q_F$ (sccm) | $Q_{HP}$ (sccm) | $Q_{LR}$ (sccm) | $t_{FE}$ or $t_{PU}$ (s) |
|---|---|---|---|---|---|
| 1 (Base Case) | ***0.0135*** | 583.6 | ***10.63*** | ***150*** | ***45*** |
| 2 | 0.0139 | 572.1 | 9.97 | ***300*** | 45 |
| 3 | 0.0138 | 585.1 | 9.79 | ***450*** | 45 |
| 4 | 0.0136 | 580.3 | 9.81 | ***600*** | 45 |
| 5 | 0.0137 | 580.8 | 9.83 | ***750*** | 45 |
| 6 | 0.0136 | 583.9 | 9.89 | ***900*** | 45 |
| 7 | 0.0135 | 586.3 | 10.83 | 150 | ***20*** |
| 8 | 0.0135 | 584.6 | 10.51 | 150 | ***30*** |
| 9 | 0.0130 | 601.3 | 10.34 | 150 | ***60*** |
| 10 | 0.0139 | 573.3 | 10.28 | 150 | ***75*** |
| 11 | 0.0139 | 575.0 | 10.27 | 150 | ***95*** |
| 12 | 0.0141 | 567.2 | 10.29 | 150 | ***110*** |
| 13 | 0.0136 | 578.8 | ***6.85*** | 150 | 45 |
| 14 | 0.0135 | 587.9 | ***14.35*** | 150 | 45 |
| 15 | 0.0138 | 577.1 | ***19.04*** | 150 | 45 |
| 16 | ***0.0093*** | 575.6 | 10.40 | 150 | 45 |
| 17 | ***0.0120*** | 576.4 | 10.14 | 150 | 45 |
| 18 | ***0.0167*** | 581.8 | 10.45 | 150 | 45 |
| 19 | ***0.0187*** | 587.5 | 10.75 | 150 | 45 |

Table 2. Values of the operating parameters used in Run # 1 (Base Case) to Run # 19. Parameters in bold italics in a column indicate the group of runs used to study the effect of that parameter on process performance. This table is the identical to Table 2 reported by McIntyre et al. (2010).

https://doi.org/10.1016/j.ces.2014.09.013

| Step | $V_{LR}$ | $V_F$ | $V_{HR}$ | $V_{BD}$ | $V_{HP}$ | $V_{LP}$ | $LRI$ | $HRI$ | $PI$ |
|---|---|---|---|---|---|---|---|---|---|
| $BD$ | × | × | × | ✓ | × | × | × | × | $\mathbb{R}$ |
| $FE$ | × | ✓ | ✓ | × | ✓ | × | $\mathbb{F}$ | $\mathbb{R}$ | × |
| $PR$ | × | × | × | × | × | × | × | × | $\mathbb{F}$ |
| $PU$ | ✓ | × | × | × | × | ✓ | $\mathbb{R}$ | $\mathbb{F}$ | × |

Table 3. Modus operandi of various valves and interaction models during different steps in the cycle organizer. '×' represents closed valve or nonfunctional interaction; '✓' represents open valve at designated or controlled flowrate; '$\mathbb{R}$' represents that the interaction model is recording information and '$\mathbb{F}$' represents that the interaction model is feeding back the recorded information.

https://doi.org/10.1016/j.ces.2014.09.013